Safer sun exposure

Wireless, battery-free, flexible dosimeters measure exposure to electromagnetic radiation outdoors and in clinical environments

Heo *et al.*/*Science Translational Medicine*

BIOSENSORS

Wireless, battery-free, flexible, miniaturized dosimeters monitor exposure to solar radiation and to light for phototherapy

Seung Yun Heo[1]*, Jeonghyun Kim[2]*, Philipp Gutruf[3], Anthony Banks[4,5,6], Pinghung Wei[7,8], Rafal Pielak[7,8], Guive Balooch[7,8], Yunzhou Shi[7,8], Hitoshi Araki[9], Derrick Rollo[10], Carey Gaede[10], Manish Patel[4], Jean Won Kwak[11], Amnahir E. Peña-Alcántara[12], Kyu-Tae Lee[13], Yeojeong Yun[5], June K. Robinson[14], Shuai Xu[14,15†], John A. Rogers[15†]

Exposure to electromagnetic radiation can have a profound impact on human health. Ultraviolet (UV) radiation from the sun causes skin cancer. Blue light affects the body's circadian melatonin rhythm. At the same time, electromagnetic radiation in controlled quantities has beneficial use. UV light treats various inflammatory skin conditions, and blue light phototherapy is the standard of care for neonatal jaundice. Although quantitative measurements of exposure in these contexts are important, current systems have limited applicability outside of laboratories because of an unfavorable set of factors in bulk, weight, cost, and accuracy. We present optical metrology approaches, optoelectronic designs, and wireless modes of operation that serve as the basis for miniature, low-cost, and battery-free devices for precise dosimetry at multiple wavelengths. These platforms use a system on a chip with near-field communication functionality, a radio frequency antenna, photodiodes, supercapacitors, and a transistor to exploit a continuous accumulation mechanism for measurement. Experimental and computational studies of the individual components, the collective systems, and the performance parameters highlight the operating principles and design considerations. Evaluations on human participants monitored solar UV exposure during outdoor activities, captured instantaneous and cumulative exposure during blue light phototherapy in neonatal intensive care units, and tracked light illumination for seasonal affective disorder phototherapy. Versatile applications of this dosimetry platform provide means for consumers and medical providers to modulate light exposure across the electromagnetic spectrum in a way that can both reduce risks in the context of excessive exposure and optimize benefits in the context of phototherapy.

INTRODUCTION

Ultraviolet radiation (UV) is the primary driver of skin cancers, the most common human malignancy. Collectively, basal cell carcinoma and squamous cell carcinoma of the skin account for more than 5 million cases per year at a cost of US$8.1 billion yearly (*1*). In 2018, there will be an estimated 90,000 new cases of melanoma, causing 9000 deaths yearly in the United States (*2*). Skin cancer is reaching epidemic proportions in the United States (*2*, *3*). In the United States, 69% of youths and 34% of adults recall at least one sunburn in the last year (*1*). Currently, there is a critical need for technologies that can accurately measure and promote safe UV exposure at a personalized level in naturalistic environments. This is particularly relevant in high-risk groups including kidney transplant survivors who have a 65 times increased risk of certain skin cancers (*4*), the 1 million melanoma survivors in the United States who have a ninefold increased risk of developing a second melanoma (*5*, *6*), and people living with rare photosensitizing skin conditions (oculocutaneous albinism, cutaneous lupus erythematosus, and porphyria cutanea tarda).

UVB (280 to 315 nm) and UVA (315 to 400 nm) are the most relevant spectral ranges in the solar UV spectrum. Although both UVB and UVA are carcinogenic and contribute to skin aging (*7*), UVB is 1000 times more erythrogenic, with distinct biological effects to the skin compared to UVA irradiation (*8*), suggesting the need for differentiation of irradiances across the UV radiation spectrum. Beyond UVB and UVA, visible and infrared (IR) radiation in sunlight can lead to oxidative stresses that potentiate UV injury, skin darkening, and skin redness (*9*–*11*). Recent studies suggest that human circadian rhythm is highly sensitive to blue light exposure, affecting sleep cycle and alertness (*12*–*14*). These collective effects motivate the need for technologies that enable the precise quantification of natural sunlight exposure not only broadly across the UV range but also with wavelength-specific resolution that extends into the visible and IR regimes at a personal and actionable level. Devices of this type could allow consumers to modulate their sun exposure

[1]Department of Biomedical Engineering, Center for Bio-Integrated Electronics, Simpson Querrey Institute for BioNanotechnology, Northwestern University, Evanston, IL 60208, USA. [2]Department of Electronics Convergence Engineering, Kwangwoon University, Seoul 01897, Republic of Korea. [3]Department of Biomedical Engineering, Bioscience Research Laboratories, University of Arizona, Tucson, AZ 85721, USA. [4]Center for Bio-Integrated Electronics, Simpson Querrey Institute for BioNanotechnology, Northwestern University, Evanston, IL 60208, USA. [5]Frederick Seitz Materials Research Laboratory, Department of Materials Science and Engineering, University of Illinois at Urbana-Champaign, Urbana, IL 61801, USA. [6]Department of Physics, University of Illinois at Urbana-Champaign, Urbana, IL 61801, USA. [7]L'Oréal Tech Incubator California Research Center, San Francisco, CA 94105, USA. [8]L'Oréal Tech Incubator, Clark, NJ 07066, USA. [9]Electronic and Imaging Materials Research Laboratories, Toray Industries Inc., Otsu, Shiga 520- 0842, Japan. [10]Carle Foundation Hospital, Urbana, IL 61801, USA. [11]Department of Mechanical Engineering, Center for Bio-Integrated Electronics, Simpson Querrey Institute for BioNanotechnology, Northwestern University, Evanston, IL 60208, USA. [12]Department of Materials Science and Engineering, Massachusetts Institute of Technology, Cambridge, MA 02139, USA. [13]Department of Physics, Inha University, Incheon 22212, Republic of Korea. [14]Department of Dermatology, Feinberg School of Medicine, Northwestern University, Chicago, IL 60611, USA. [15]Departments of Materials Science and Engineering, Biomedical Engineering, Chemistry, Mechanical Engineering, Electrical Engineering and Computer Science, and Civil and Environmental Engineering, Center for Bio-Integrated Electronics, Simpson Querrey Institute for BioNanotechnology, Northwestern University, Evanston, IL 60208, USA.
*These authors contributed equally to this work.
†Corresponding author. Email: stevexu@northwestern.edu (S.X.); jrogers@northwestern.edu (J.A.R.)

based on individual activities, geographic locations, time of day, skin type, and medical conditions. The result would enable informed engagement in sun-protective behaviors specific to the individual and their microenvironment before the development of clinically evident skin erythema, such as increasing sunscreen use or seeking shade.

Current approaches to individualized monitoring focus only on UV, typically including both UVA and UVB in a single combined measurement, and require wearables in the form of badges or wristbands. Conventional, battery-powered electronics in these systems facilitate wireless operation and digital data collection using photodetectors and memory modules, where collective costs can be excessive. Furthermore, the limited lifetimes of the batteries, their need for recharging, and their susceptibility to heat, water, and other environmental conditions hinder usability, typically leading to device abandonment (*15*–*17*). Certain traditional wearables designed primarily for other purposes offer UV sensing as additional functionality with incremental costs but with the same drawbacks as specialized dosimeters (*18*). The devices adopt form factors that require straps to the wrist, chest, or waist or that require clips that affix to clothing or personal accessories. In all cases, the necessary protective packaging for the complex assembly of electronics provides only modest protection against water immersion and physical impact. Robust functionality during water recreation and outdoor sports is critical because of the increased risks of sunburn and excessive UV exposure. The shortcomings of these devices lead to improper or discontinued use by consumers or prevent adoption. Devices in practice have limited utility in minimizing risks of overexposure, sunburn, and skin cancer.

As an alternative that addresses some of these deficiencies, recent research demonstrated capabilities in quantitative, continuous exposure monitoring using thin, skin-like patches that incorporate colorimetric chemical reagents for UV dosimetry (*19*). Although these systems overcome certain drawbacks of conventional digital devices, their accuracy is limited by the colorimetric nature of the measurement, and they are restricted to single-use operation. A critical unmet need is a broadly adoptable, low-cost, miniaturized, and accurate system to enable informed protection from the sun, ideally with a continuous and accumulative mode of digital measurement at multiple discrete wavelength bands, with data analysis algorithms and user-responsive software interfaces capable of influencing healthy behavior that can be deployed on multiple parts of the body.

Here, we introduce a millimeter-scale, wireless, and battery-free platform with versatile operational schemes for dosimetry. The operational schemes include single- to multiple- wavelength dosimetry across a wide range of the electromagnetic spectrum (UV to IR), instantaneous measurements of intensity in real-time with visual indicators linked to exposure thresholds, and simultaneous digital readings of skin and/or environmental temperature. Foundational advances in near-field communication (NFC) technologies, antenna layouts, and manufacturing approaches in flexible electronics and electronic circuit design underpin these systems. We demonstrate UVA, UVB, visible, and IR radiation monitoring, cumulatively and instantaneously, individually and collectively, where devices are mounted on human participants during outdoor activities (including aquatic environments), in therapeutic phototherapy units, and during blue light phototherapy in operating neonatal intensive care units (NICUs).

RESULTS

An illustrative example consists of a simple, miniaturized platform (Fig. 1A) that measures surface temperature and UVA exposure dose in a battery-free, continuous accumulation mode (*20*–*22*). NFC-enabled hardware (smartphones, tablets, and personal computers) wirelessly coupled to the device displays user-specific total exposure dosage at a single wavelength (fig. S1). The diameter, thickness, and weight of the device are 8.0 mm, 1.1 mm, and 51.2 mg, respectively. The components (Fig. 1B) of this millimeter-scale NFC (mm-NFC) platform include the following: a system on a chip (SoC) with NFC functionality and an integrated temperature sensor; a dual-coil, magnetic resonant radio frequency (RF) antenna; a photodiode (PD) with narrowband response aligned to the UVA region of the spectrum; a supercapacitor (SC); and an n-channel metal oxide semiconductor field-effect transistor (MOSFET). The antenna and the thinned, bare-die NFC SoC (thickness, 200 μm) provide a two-way wireless interface for data extraction, power transfer, and external control. The PD generates a photocurrent with a magnitude that correlates with the instantaneous exposure intensity and its wavelength-dependent external quantum efficiency (EQE). The resulting photocurrent continuously charges the SC, which connects to the PD in a parallel arrangement, throughout a period of exposure. The accumulated charge on the SC is a function of exposure dose. This SC interfaces to an analog-to-digital converter (ADC) embedded within the SoC. Wireless readout involves the transmission of the voltage that develops on the SC via the digital output from the ADC. A calibration factor converts the raw voltage measurement to cumulative exposure dose. Wireless activation of a general-purpose input/output (I/O) port on the SoC supplies a 1.5-V signal to the gate of the MOSFET, which discharges the SC and thereby resets the device. This reset approach can extend the detection range for exposure dose without bound. Extraction of temperature measurements occurs through the same wireless link.

Devices were fabricated by following a simple set of procedures using a laser structuring tool, a galvanic pulsed electroplating system, and a pick-and-place machine. The substrate is a thin, flexible sheet of polyimide (PI; thickness, 75 μm) clad in rolled and annealed copper (thickness, 18 μm) (Fig. 1C). The thickness of the completed system varies from a maximum at the location of the SC (1.0 mm) to a minimum value at the bare regions of the PI. A transparent coating of poly(dimethylsiloxane) (PDMS) or UV-transparent optical adhesive [Norland Optical Adhesive (NOA)] applied to the entire device in liquid form spontaneously forms into a smooth, continuously curved shape through the action of surface tension that, after thermal or photo curing, yields a solid material that fully encapsulates the active components to isolate them from the surroundings with a waterproof seal. PDMS offers a soft, flexible package, whereas the NOA provides a hard, rigid, mechanically static construction.

The miniaturized dimensions, the lack of switches, the absence of interface ports, and the purely solid-state operation facilitate use in multiple activities, including during complete immersion in water, on nearly any region of the body, on clothing, jewelry, and accessories, or on other device platforms. As reported in other contexts (*20*), mechanically bending the antenna structures over a relevant range maintains a stable RF operation near 13.56 MHz, compliant with the NFC protocol. Many wearable modes exist, including integration as sunglasses accessory (Fig. 1D), onto fingernails or thumbnails (Fig. 1E), skin-mounted patches (Fig. 1, F and G, and fig. S2A), earrings (Fig. 1H), wristlets (Fig. 1I), shoe clips (fig. S2B), hair clips (fig. S2C), shirt buttons (fig. S2E), hats (fig. S2E), or rings. The encapsulation layer

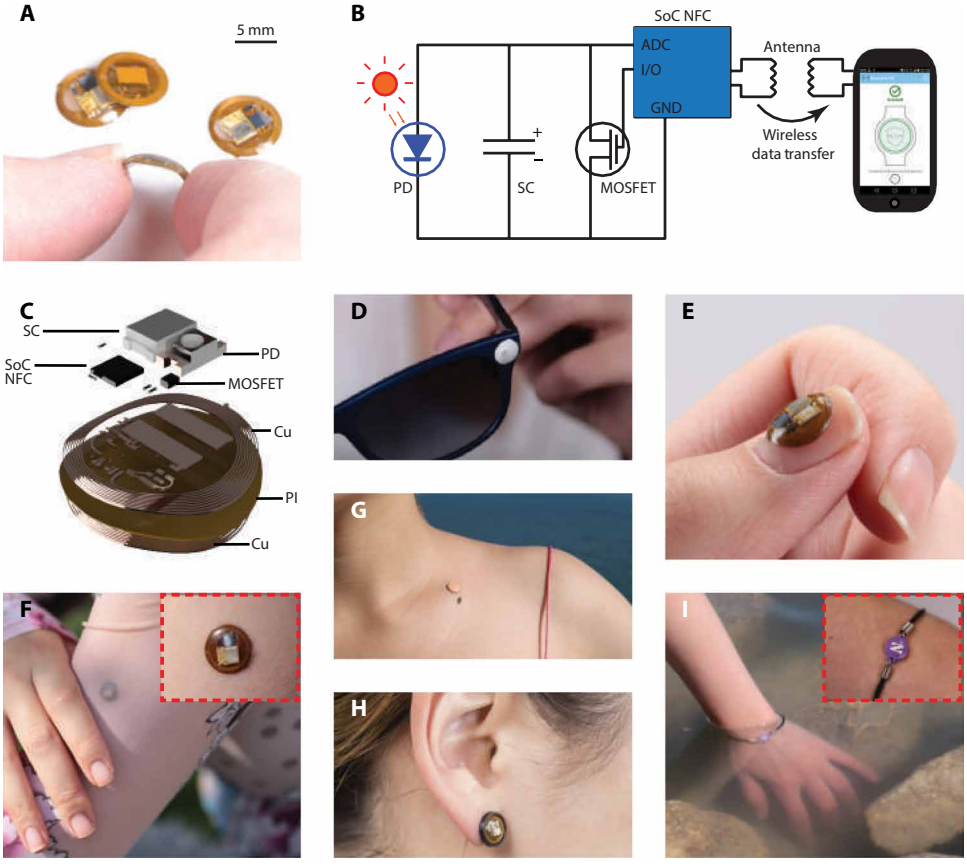

Fig. 1. Millimeter-scale, battery-free, wireless sensors of UVA radiation. (**A**) Photographic images of a dosimeter for measuring UVA exposure dose in a continuous accumulation mode, bent between the thumb and index finger. The diameter, thickness, and weight of the device are 8 mm, 1.5 mm, and 110 mg, respectively. Images of the other three dosimeters show the front and back of the device. (**B**) Circuit diagram of the system and its wireless interface to a smartphone. The NFC chip, the MOSFET, the SC, and the photodetector are labeled NFC, MOS, SC, and PD, respectively. GND indicates ground. (**C**) Schematic, exploded view illustration of the constituent layers: the RF antenna (Cu coil), the NFC chip (NFC), the passive components, the UVA photodetector (PD), the SC (SC), and the insulating film (PI). (**D** to **I**) Photographic images demonstrating the flexibility of the sensor on various body parts, materials, and form factors. Insets in (F) and (I) show higher-magnification images.

serves as a convenient canvas for incorporating various color graphic designs, provided that a transparent window remains at the position of the PD.

Indoor characterization of mm-NFC UVA dosimeters

A narrowband UVA lamp with peak emission wavelength at 365 nm served as a controlled exposure source for indoor testing (fig. S3A). Measurements using a UVA photometer with specified accuracy of ±10% defined the reference intensities for each exposure condition. Time integration of exposure intensities yielded reference cumulative dose values. The EQE characteristics of the UVA PD define the spectral sensitivity of the dosimeter (Fig. 2A). The UVA PD has a peak EQE at ~350 nm with a full width at half maximum (FWHM) of ~50 nm. Two types of charge flow determine the sensitivity and accuracy of accumulation mode dosimetry: photocurrent generated by the PD and collective, parasitic leakage currents from the SC, PD, MOSFET, and ADC of the SoC. The photocurrent generated by the UVA PD is linearly proportional to the exposure intensity of UVA [R^2 = 0.99, slope: 158 ± 4 nA $(mW/cm^2)^{-1}$; Fig. 2B]. Consequently, the rate of charging the SC is directly proportional to the intensity of UVA exposure (fig. S3B). The measured, system-level leakage currents, as determined by the applied current necessary to maintain the voltage at a fixed value in dark conditions for SC voltages from 50 to 250 mV (Fig. 2C), showed increasing leakage currents with SC voltage. At SC voltages of 50 and 200 mV, leakage currents were 9 ± 5 nA and 33 ± 6 nA, respectively. The leakage measurements of individual components PD (Fig. 2D), MOSFET (Fig. 2E), and ADC of SoC (fig. S3C) showed low leakage currents (<10 nA), independent of voltage across the SC. In contrast, the SC had high leakage currents of 12 ± 1 nA and 32 ± 3 nA at bias values of 50 and 200 mV, respectively, and primarily contributed to the system-level leakage (Fig. 2F). The total leakage was captured accurately using these component-level measurements, together with a simple LTspice (simulation program with integrated circuit emphasis) model (fig. S3D) of the circuit that uses idealized components, with leakage simulated by a resistor. The results matched experimentally observed behavior (fig. S3E), thereby establishing the model as a guide for the development of alternative designs. In practical use, each wireless data extraction process can occur with a reset command to maintain low SC voltage and to thereby minimize leakage.

The voltage outputs of an mm-NFC UVA dosimeter as a function of reference cumulative exposure dose (Fig. 2G), exposed with constant intensity over time at six different irradiances (fig. S3B), exhibited a linear charging behavior with a slope of 21 ± 1 mV $(J/cm^2)^{-1}$. A reader antenna wirelessly captures data with a resolution of 1 mV (defined by the ADC on the NFC SoC). The mm-NFC dosimeter demonstrated a linear charging behavior up to 200 mV (fig. S3F), beyond which the parasitic leakage current of SC degraded the charging rate (fig. S3G). For accurate dosimetry, a wireless reset activation to maintain SC voltage below 200 mV is recommended. The voltage outputs from an mm-NFC UVA dosimeter as a function of exposure energy measured at increasing temperatures (fig. S3, H and I) indicated ~3 and ~6% variations in charging rate at 38° and 50°C, respectively, compared to room temperature (23°C). The temperature sensor onboard the SoC presents an option to calibrate the charge rate conversion via parallel temperature monitoring, if necessary.

As previously mentioned, the SoC also features an integrated temperature sensor. Simultaneous monitoring of temperature and UVA exposure dose with an mm-NFC device (Fig. 2H) indicated reliable UVA dosimetry, temperature sensing, and wireless communication underwater from room temperature to 50°C. An NOA-encapsulated

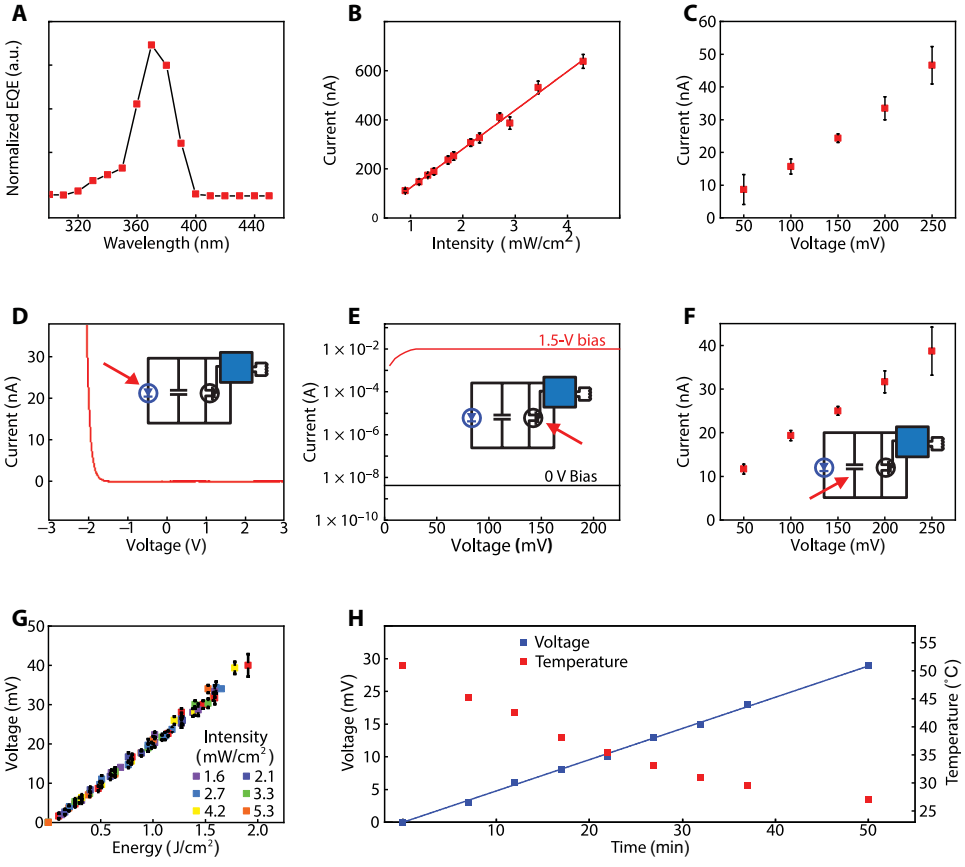

Fig. 2. Indoor characterization of millimeter-scale, battery-free UVA dosimeters. (**A**) EQE of the UVA PD ($n = 1$). a.u., arbitrary units. (**B**) Mean photocurrent from the UVA PD ($n = 3$) as a function of the intensity of UVA exposure. The error bars represent SDs. (**C**) Mean system-level leakage current of dosimeter ($n = 3$) at increasing SC voltage in the dark. Measured leakage current is the current needed to maintain a constant voltage across SC. The error bars represent the SD. (**D**) Current-voltage response of the UVA diode ($n = 1$) measured in the dark. The inset is the circuit diagram of the system with an arrow indicating the UVA diode. (**E**) Drain current of the MOSFET ($n = 1$) at ON (1.5 V) and OFF (~0 V) gate biases as a function of voltage. The inset is the circuit diagram of the system with an arrow indicating the MOSFET. (**F**) Mean leakage current associated with the SC ($n = 3$). The error bars represent the SD. The inset is the circuit diagram of the system with an arrow indicating the SC. (**G**) Mean voltage output as a function of cumulative dose of UVA exposure. Dosimeter ($n = 3$) was irradiated with constant intensity over time at six different intensities. The error bars represent the SD. (**H**) Voltage output as a function of time of UVA exposure with constant intensity, as the device ($n = 1$) submerged in water is cooled from 50°C to room temperature over 50 min. Voltage and temperature readouts were wirelessly obtained every 5 min with an NFC reader antenna.

UVA dosimeter immersed in heated water was exposed to constant intensity of UVA as the water cooled from 50°C to room temperature (fig. S3I). The reader antenna, under the beaker containing the device (fig. S3J), wirelessly acquired voltage and temperature every 5 min. The devices were resistant to water exposure, suggesting reliable performance during heavy sweating scenarios and in aquatic activities. Ten dosimeters encapsulated in NOA and mounted on fabric swatches (fig. S3K) inserted in a washing machine rotating at 400 rpm with 40°C water for 35 min remained fully functional.

Performance of mm-NFC UVA dosimeters in real-world conditions

To test the functionality and wearability of dosimeters under different environmental conditions, one set of field trials involved nine healthy volunteers engaged in recreational activities during a 4-day period in Rio, Brazil. mm-NFC UVA dosimeters were worn on the thumbnail or the middle fingernail, depending on personal preference, and commercial dosimeters were worn on the wrist of the ipsilateral side. The participants took part in recreational activities on a rooftop from 9 a.m. to 4 p.m., corresponding to solar zenith angles from 50°E to 60°W. Voltage output of the mm-NFC dosimeters as a function of exposure dose determined using the commercial devices at corresponding times (Fig. 3A and fig. S4) showed a linear correlation [$R^2 = 0.94$, slope: 8.8 ± 0.2 mV $(mJ/cm^2)^{-1}$]. In a second study in the same geographic location, the participants engaged in diverse activities in and around a pool from 8 a.m. to noon, including showering and swimming with the use of soap and skin creams. The data (Fig. 3B) show a wide range of accumulated doses (29 to 300 mV), as expected on the basis of the differences in behaviors. These observations imply highly variable UV-associated risks between participants, due not only to differences in Fitzpatrick skin types but also to individual behavior patterns. The results highlight the need for personalized dosimetry. In both studies, all sensors remained functional throughout the testing. Over the 4 days of the study, 14 of 20 devices remained strongly adhered to the fingernail.

An additional set of field trials in St. Petersburg, Florida involved 13 healthy volunteers, each with skin-mounted mm-NFC UVA dosimeters on the right back hand (RBH), left back hand (LBH), left inner arm (LIA), and left outer arm (LOA) and with a commercial dosimeter (Scienterra) on the right wrist (Fig. 3C). Here, participants walked a 6.44-km path in the morning from 10 a.m. to 12 p.m., in the afternoon from 1 p.m. to 3 p.m., and in the evening from 4 p.m. to 6 p.m., with wireless measurements captured every 30 min via a smartphone. The 6.44-km track extends approximately 1.61 km in each of the cardinal directions (Fig. 3D). Figure 3E and fig. S5 show results from four different patch locations. Four devices failed during the afternoon exercise after the morning exercise. The evening walk occurred 4 days later. Exposure recordings from the LBH and LOA are similar. Results from the LIA, often a skin area used to determine Fitzpatrick skin type due to minimal tanning effects, recorded the least exposure, as expected. Figure 3 (F and G) are box-and-whisker plots of measurements obtained from dosimeters on the LBH and RBH during the walk composing of 1 mile north, east, west, then south. The sun is in the east in the morning, and devices on the RBH measured larger doses than those on the LBH as participants walked north, whereas smaller doses were measured as participants walked south (Fig. 3F). During the evening, the sun is in the west, and the reverse is true (Fig. 3G).

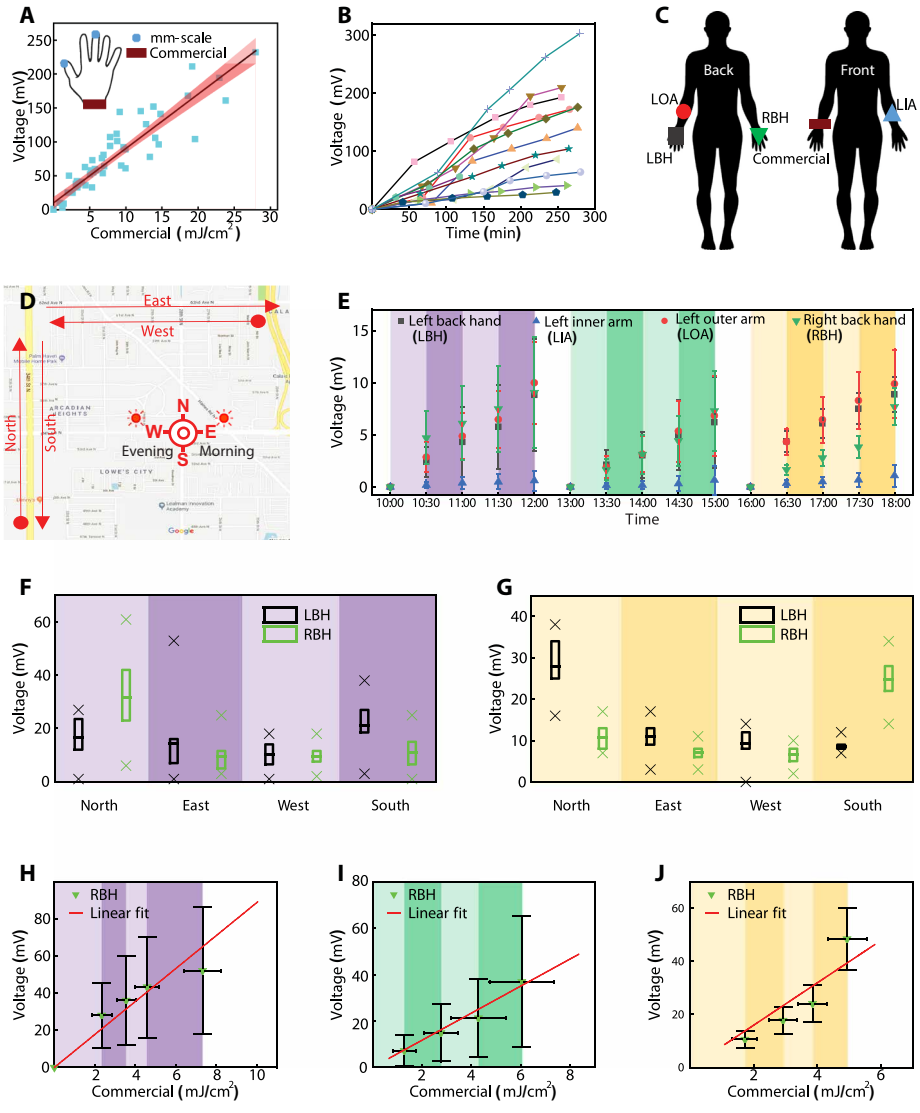

Fig. 3. Outdoor characterization of millimeter-scale, battery-free UVA dosimeters. (**A**) Comparison of mm-NFC UVA dosimeter measurements to those of a standard commercial dosimeter from Scienterra. The graph includes a linear fit and a 95% confidence interval (shading). The measurements are from a field trial in Rio, Brazil on 10 March 2016. Participants ($n = 8$) wore one mm-NFC UVA dosimeter on the thumbnail or the middle fingernail, and one commercial dosimeter on the right wrist (inset). Participants collected data every hour while engaging in recreational activities of their preference on a roof top from 8 a.m. to 3 p.m. (**B**) mm-NFC dosimeter measurements from participants ($n = 12$) in Rio, Brazil engaged in water activities at a pool. (**C**) Schematic illustration of study participants wearing four mm-NFC UVA dosimeters as skin-mounted devices on LBH, LOA, LIA, and RBH and one commercial dosimeter on the right wrist. (**D**) Map of a ~6.44-km predetermined path in St. Petersburg, Florida. Participants performed wireless measurements with a smartphone after walking north (N), east (E), west (W), and south (S) in the morning (sun in the east), in the afternoon (sun at zenith), and in the evening (sun in the west). (**E**) Mean dosimetry measurements using mm-NFC UVA devices as a function of time during a trial in St. Petersburg, Florida (August, 2016). Participants acquired wireless measurements from four mm-NFC UVA dosimeters on the LBH, LIA, LOA, and RBH as in (C) every 30 min (shading) with a smartphone during morning (purple; $n = 13$), afternoon (green; $n = 9$), and evening (yellow; $n = 11$) exercise sessions. Morning and afternoon exercise took place on the same day, and the evening exercise occurred 4 days later. The presented data omit four measurements from failed devices taken from an afternoon exercise. The error bars correspond to SDs. (**F**) Box-and-whisker plot with minimum, maximum (25%, 75% percentile) and mean of mm-NFC dosimeter measurements from RBH and LBH of participants ($n = 13$) taken from a morning exercise. (**G**) Box-and-whisker plot with minimum, maximum (25%, 75% percentile) and mean of mm-NFC dosimeter measurements from the RBH and LBH of participants ($n = 9$) captured during an afternoon exercise. Comparison of measurements collected outdoors during (**H**) morning ($n = 13$), (**I**) afternoon ($n = 9$), and (**J**) evening ($n = 11$) exercises using mm-NFC dosimeters to those obtained with a commercial dosimeter. Graphs show averages of measurements acquired after walking north, east, west, and south and linear fits of collected data. The error bars represent SDs.

Figure 3 (H to J) compare results from mm-NFC UVA dosimeters on the RBH to measurements from commercial dosimeters on the wrist during morning ($n = 13$), afternoon ($n = 9$), and evening ($n = 11$) walks, respectively. Plots show averages of measurements acquired after walking north, east, west, and south and linear fits of the collected data (figs. S6 to S8). The results from the morning, afternoon, and evening show linear correlations ($R^2 = 0.80$, $R^2 = 0.67$, and $R^2 = 0.88$, respectively). Slopes from results after the morning [8.9 ± 0.6 mV $(mJ/cm^2)^{-1}$] and evening [8.0 ± 0.5 mV $(mJ/cm^2)^{-1}$] walks are similar to those derived from the studies in Brazil [8.8 ± 0.2 mV $(mJ/cm^2)^{-1}$]. Slopes from results collected during the walk in the afternoon [5.8 ± 0.7 mV $(mJ/cm^2)^{-1}$] are smaller. This result can be understood by considering the angles of solar illumination at the dosimeters. The solar zenith angles during morning, afternoon, and evening activities range approximately from 65°E to 40°E, 30°E to 20°E, and 30 W° to 50 W°, respectively. Compared to morning and evening, UVA radiation is inefficiently captured by the mm-NFC devices on the RBH in the afternoon because of the steep, off-normal angle of incidence relative to the surface of the PD (fig. S4I). The optical diffuser present in the commercial dosimeters enhances the detection efficiency compared to that of the mm-NFC, thereby reducing the slope. By similar reasoning, the slopes from all field results are smaller than those from indoor calibration [21 ± 1 mV $(J/cm^2)^{-1}$; Fig. 2G], where the illumination from the UV lamp occurs at normal incidence and off-axis illumination is negligible.

These studies highlight the differences between mm-NFC dosimeters and commercial devices in real-world, practical scenarios. The former operate in continuous, uninterrupted modes, whereas the latter capture instantaneous values of intensity at preprogrammed intervals and then yield an effective value for cumulative exposure by time integration, with the assumption that the intensity varies linearly between measurements. As a result, fluctuations of UV intensity that occur at rates faster than the sampling frequency can lead to errors in the measurement (fig. S9). For instance, commercial dosimeters at the wrist can experience rapid changes

in UV radiation due to shadowing effects, especially during active body motion.

mm-NFC dosimeters with dual UVA/UVB operation

The mm-NFC UVA/UVB dosimeter (Fig. 4A) has a diameter, thickness, and weight of 16 mm, 1.5 mm, and 500 mg, respectively. The layout (Fig. 4B) is configured for simultaneous dosimetry in the UVA and UVB regions of the solar spectrum, bands that are known to have drastically different health consequences and safe exposure doses. Separate ADCs embedded in the SoC allow independent modalities in dosimetry. Similar to the design of the mm-NFC UVA dosimeter, here, two separate ADCs interface to two SCs that connect in parallel to separate UVA and UVB PDs, with two MOSFETs controlled by a single general purpose input/output (GPIO) for reset. Each sensing channel is independently optimized, calibrated, and designed to measure various wavelengths of interest. An array of UVB PDs, to account for an intensity in the UVB region that is 100 times less than that in the UVA because of partial absorption of UVB radiation by the ozone layer (*23*), ensures adequate charging rates during solar exposure.

The EQE characteristics of the UVB PD (Fig. 4C) indicate that the maximum efficiency is at 305 nm and that the FWHM is ~28 nm. A narrowband UVB lamp with peak emission wavelength of 305 nm served as a controlled exposure source for indoor testing. Similar to the approach for testing the mm-NFC UVA dosimeter, a UVB photometer with specified accuracy of ±10% defined the reference intensity for each exposure condition. The voltage output of mm-NFC UVB channel of the UVA/UVB dosimeter as a function of reference cumulative dose for devices that incorporate 10 UVB PDs, 4 PDs, and 1 PD (Fig. 4D) illustrates the scaling of the response with the number of PDs. Increasing the number of PDs effectively increases the sensitivity, with calibration factors of 8, 24, and 71 mJ/cm^2 per 1 mV for devices with 10 UVB PDs, 4 PDs, and 1 PD, respectively. The output photocurrent as a function of UVB intensity for varying numbers of UVB PDs (Fig. 4E) and the system-level leakage for these devices (Fig. 4F) showed that photocurrent scales with numbers of PDs, whereas leakage currents for dosimeters that incorporate 10 and 1 PDs are similar at low SC voltages (<200 mV). Because the semiconductor components of the system contribute minimally to the overall leakage current, the sensitivity to UVB can be increased in a straightforward manner through the addition of corresponding PDs.

During exposure involving (i) both UVA and UVB lamps, (ii) only the UVB lamp, or (iii) only the UVA lamp, the UVA and UVB intensities were 1.4 and 0.16 mW/cm^2, respectively, to simulate typical low-index UV conditions outdoors (Fig. 4G). To observe the effects of leakage, the reset was not activated at any point during the experiments. As expected, measurements of cumulative UVB dose exhibited a constant slope during phases 1 and 2 (R^2 = 0.99). Similarly, results for cumulative UVA dose exhibited a constant slope in phases 1 and 3 (R^2 = 0.99). The reading from the UVB dosimeter increased by a small amount during phase 3 because of a slight overlap of the EQE of the UVB PD with the spectral range of the UVA lamp. The constant slopes and the stable plateaus are consistent with negligible leakage during the practical measurement scenarios examined here.

In addition to applications in solar UV exposure, these same devices can be deployed in clinical settings of relevance to UVA/UVB phototherapies, which represent the current standard of care for patients with common inflammatory skin conditions such as psoriasis and atopic dermatitis. Demonstrations of mm-NFC UVA/UVB dosimeters in UVA/UVB phototherapy units involving five devices (fig. S10A) positioned along a vertical axis of a cylindrical tube,

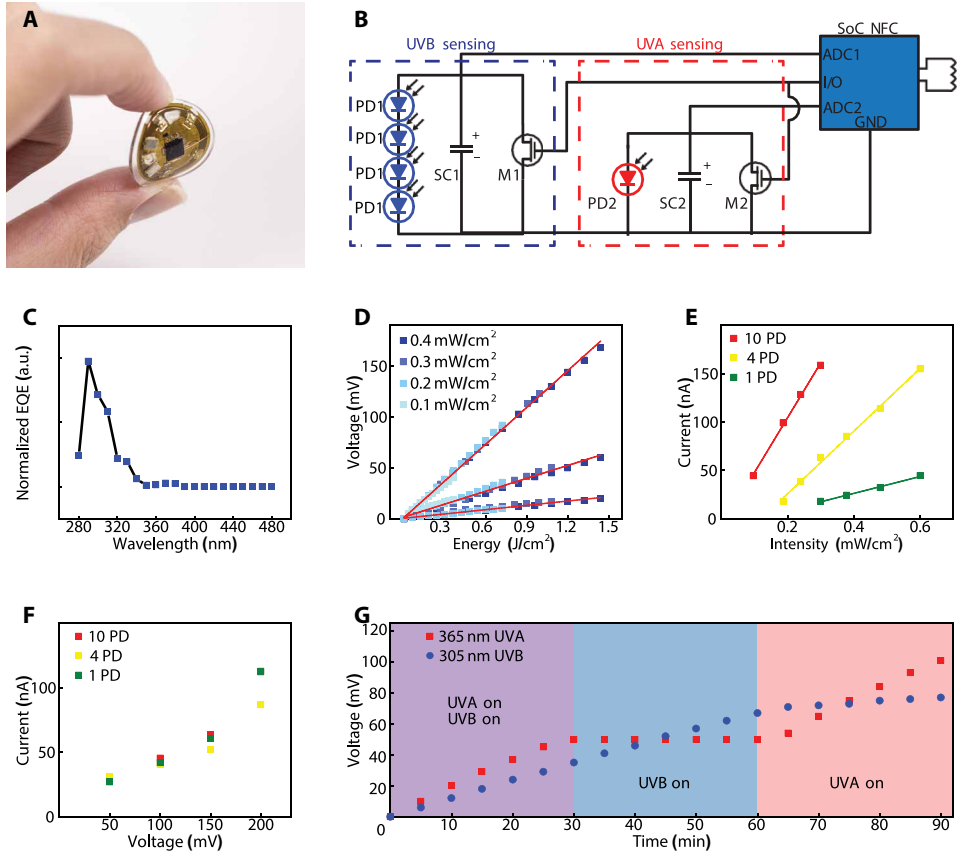

Fig. 4. mm-NFC dosimeters with dual, independent operation in the UVA and UVB ranges. (**A**) Photographic image of a dosimeter capable of independent measurements of UVA and UVB, bent between a thumb and index finger. (**B**) Circuit diagram of the device. The configuration follows that of the UVA dosimeter but using two separate ADCs on a single NFC chip, two SCs (SC1, SC2), two MOSFETs (MOS2), and single GPIO for reset, and separate UVA PD (PD2) and UVB PDs (PD1 × 4). (**C**) EQE spectrum of a UVB PD (n = 1). (**D**) Output of the UVB dosimeter channel as a function of total dose of UVB (305 nm) exposure. Measurements show results for dosimeter that incorporate 10 UVB PDs (PDs), 4 PDs, and 1 PD to illustrate the scaling of the response (n = 1). (**E**) Photocurrent as a function of intensity of UVB (305 nm) exposure for dosimeters with 10 PDs, 4 PDs, and 1 PD (n = 1). (**F**) System-level leakage current of the dosimeter (n = 1). Measured leakage current is the current to maintain constant voltage. (**G**) Output voltages from the UVA and UVB channels (n = 1) as a function of time of exposure to a combination of UVA (365 nm) and UVB (305 nm), only UVA, or only UVB. The UVA intensity is 2.2 mW/cm^2, and the UVB intensity is 0.16 mW/cm^2.

corresponding to different anatomical locations (head, shoulder, waist, knee, and shin), showed spatially resolved exposure information (fig. S10B). The results also revealed time-dependent behavior during lamp warm-up (fig. S10C). Multiple mm-NFC devices deployed in this manner could facilitate the optimization of treatment doses at targeted areas of the skin. The spatiotemporal measurement capabilities (fig. S10, D and E, and tables S1 to S4) also have utility in home-based UV therapy. Patients can monitor not only their cumulative UV exposure outdoors throughout the day but also their UV phototherapy exposure at home around targeted, localized areas of the skin that remain recalcitrant.

mm-NFC dosimeters for blue light phototherapy in neonates in NICUs

Another area of clinical application involves the use of mm-NFC dosimeters with spectral sensitivity matched to the output of blue lights deployed in newborn nurseries and NICUs (*24*). The resulting information could allow physicians and nurses to optimize treatment protocols for phototherapy of jaundiced infants. The American Academy of Pediatrics establishes guidelines of the minimum phototherapy intensity for the treatment of jaundiced neonates. Standard phototherapy for infants with moderate and severe bilirubinemia requires intensities greater than 10 and 30 $\mu W/cm^2$, respectively (*25*). In spite of these guidelines, protocols for monitoring of blue light intensities both before and during exposure at the skin level of the neonate are highly variable.

Clinical studies demonstrated the potential utility of mm-NFC blue light dosimeters in optimizing delivery of therapeutic light for neonates, aimed to reduce the time for phototherapy treatment and decrease the risk of kernicterus (*25*), a complication where bilirubin deposits in the brain cause permanent neurological damage. Encapsulating mm-NFC devices with soft, skin-safe formulations of PDMS yielded robust, lightweight devices that can reversibly integrate directly with the skin of the neonate in a safe, noninvasive fashion. Blue light dosimeters capable of cumulative dosimetry have an integrated red light-emitting diode (LED) that wirelessly activates when the exposure intensity exceeds 30 $\mu W/cm^2$ (Fig. 5A). In addition to features common to the cumulative sensing devices (SC, PD, and MOSFET; Fig. 1A), these dosimeters provide instantaneous sensing functionality. Specifically, the voltage response of a PD and the amplifier (Amp) interfaces to an ADC. The amplified voltage response is directly proportional to exposure intensity. The amplified PD signal also passes to the gate of the MOSFET (M2), which has a threshold voltage of 850 mV. Proper selection of the resistor (R1) and the capacitor (C1) leads to voltages capable of switching M2 to its ON state, thereby activating a red indicator LED connected in series, for blue light intensities of 30 $\mu W/cm^2$ or higher. The Amp and the LED are wirelessly powered by the antenna-rectified voltage (VDDH) generated by a reader antenna that simultaneously enables continuous wireless data transfer through the NFC communication link.

The diameter, thickness, and weight of the advanced mm-NFC blue light dosimeter (Fig. 5B) are 16 mm, 1.2 mm, and 300 mg, respectively. mm-NFC blue light dosimeters were mounted on the chest regions of jaundiced infants undergoing blue light therapy treatment (Fig. 5C). For applications in the NICU, a long-range NFC reader antenna (30 cm by 30 cm, with a reading range of 10 to 30 cm) located underneath the incubator mattress enabled continuous and automatic wireless collection of data at a programmed time interval. As reported in other contexts, the wireless communication strength depends on the orientation of the sensor with respect to the magnetic field generated by the NFC reader antenna (*26*). Wireless communication is possible for angles across a range from 0° to 80° between the antenna planes of the dosimeter and the reader. Alternative antenna geometries can be considered for blue lights that illuminate at different angles.

The EQE characteristics of the PD match the absorption spectrum of bilirubin. Here, the addition of a layer of PI (thickness, 5 μm) onto a PD with a maximum efficiency at ~380 nm shifts the maximum to ~450 nm, approximately aligned with the maximum spectral absorption wavelength of bilirubin (Fig. 5D). The FWHM is ~55 nm. In this way, the device is minimally responsive to other sources of visible light in the ambient environment. The voltage output of the mm-NFC blue light dosimeter as a function of reference cumulative dose (Fig. 5E) and as a function of reference instantaneous intensity (Fig. 5F) is linear ($R^2 = 0.99$). A standard blue light phototherapy system served as the exposure source, and a hand-held, commercial device captured the intensity at the point of exposure. The calibration factors for measurements of cumulative dosimetry and instantaneous intensity are 2.4 mJ/cm^2 per 1 mV and 0.44 $\mu W/cm^2$ per 1 mV, respectively.

Representative results from experiments with a neonate, collected throughout a typical phototherapy session, are shown in Fig. 5G (fig. S11). Here, a dosimeter without the indicator LED (Fig. 5C, inset) continuously and wirelessly measured total exposure energy and exposure intensity at a programmable interval of 20 min over 20 hours. These data indicated that the infant received treatment at intensities above the recommended value of 10 $\mu W/cm^2$ only 49% of the total time. The blue light phototherapy treatment intensity was below 10 $\mu W/cm^2$ for the remaining time, including periods (23% of the total) during which the sensor measured no incident light (attributed to failed communication attempts between the reader antenna and the device). These readings correspond to cases when (i) the device has an orthogonal, or nearly orthogonal, orientation relative to the reader antenna, (ii) the blue light phototherapy unit is deactivated temporarily, (iii) the neonate is removed from the isolette, or (iv) the path of light to the region of the sensor is blocked. The readings from the instantaneous monitor indicated ~5 hours of exposure time that corresponded to low or negligible intensities due to some combination of orientation (lying on the left or right sides) or removal from the region of illumination, with results consistent with the cumulative dosimetry measurements that continue uninterruptedly. The results from this representative phototherapy session reveal that 25% of a total 20-hour session has suboptimal blue light exposure.

mm-NFC dosimeters with operation at IR to UV wavelengths

A final set of examples illustrates the ability for monitoring from three separate sensors, in a way that fully uses the functionality available on the NFC SoC. The circuit configurations (Fig. 6A) represent straightforward extensions of previously described platforms but using three separate ADCs, three SCs arranged in parallel to separate PDs, and three MOSFETs connected to a single I/O for reset. The EQE spectra of the PDs define the bands of wavelength for operation (Fig. 6B) with a peak EQE at ~940 nm (IR) and from 558 to 618 nm (red). Linear voltage responses of the mm-NFC dosimeters as a function of cumulative exposure energy in the red and IR regions of the spectrum are shown in Fig. 6C. A UVA/UVB/IR dosimeter in

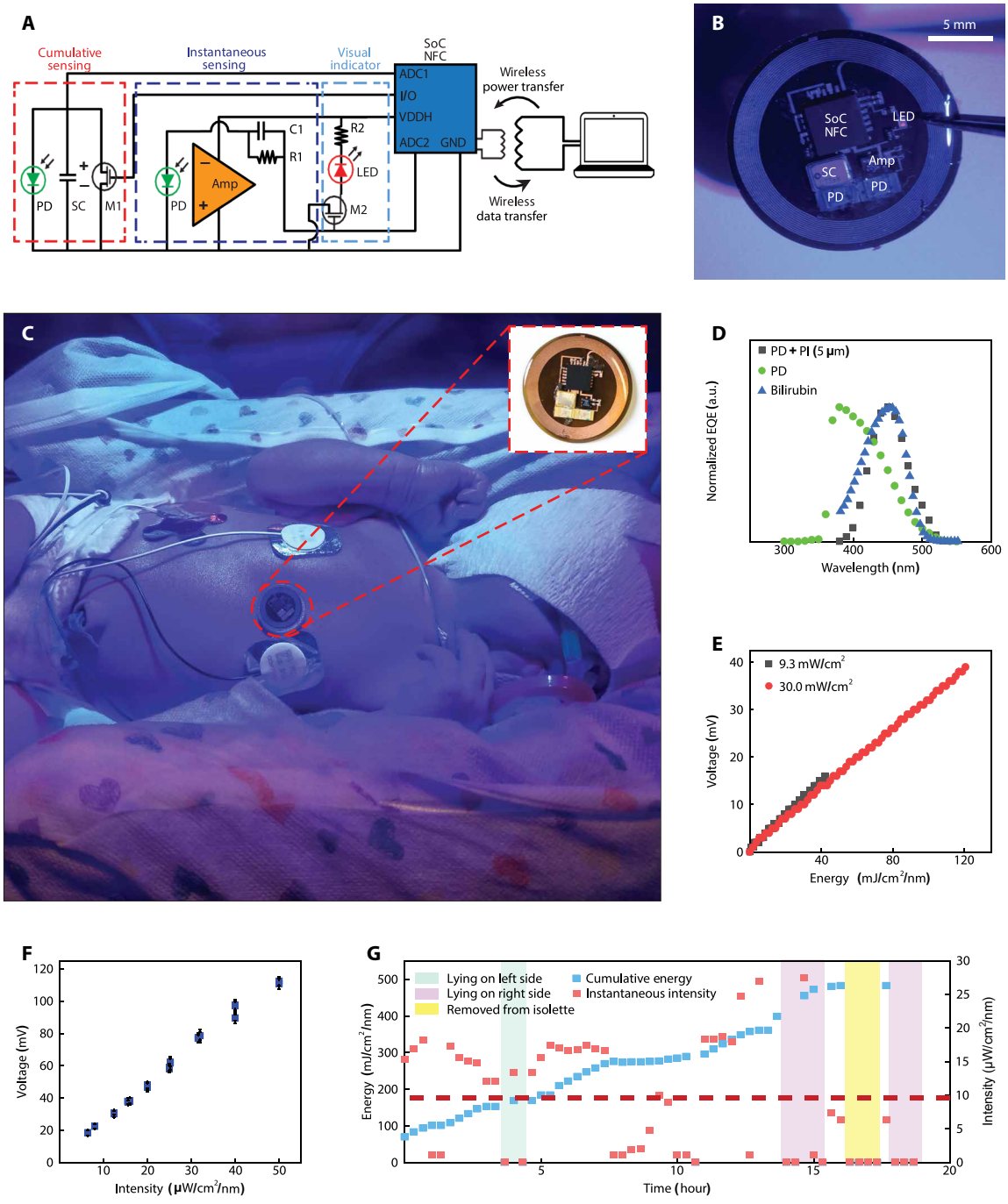

Fig. 5. mm-NFC dosimeters for blue light phototherapy in the NICU. (**A**) Circuit diagram of the device. The configuration uses ADC1 and ADC2 on a single NFC chip to feature cumulative and instantaneous sensing, respectively. The cumulative sensing circuit follows that of the UVA dosimeter, using an SC (SC1), a MOSFET (M1), and a GPIO for reset and a blue light PD (D1). The instantaneous sensing circuit couples an Amp powered by VDDH to a blue light PD (D2). The amplified voltage response of the PD passes to the gate of M2, which has a threshold voltage of 850 mV. The sensitivity of the blue light dosimeter is optimized to correspond to threshold blue light phototherapy intensity of 30 μW/cm^2. For exposure intensities 30 μW/cm^2 or higher, M2 is switched to an ON state to activate a read indicator LED connected in series. Activation of the sensor by a reader antenna leads to wireless transmission of the digital output from the ADC through the NFC communication link. (**B**) Image of a blue light dosimeter/photometer with visual indicator of intensity threshold designed for monitoring blue light phototherapy exposures in the NICU. The diameter, thickness, and weight of this encapsulated device are 16 mm, 1.2 mm, and 0.3 g, respectively. (**C**) Image of a device without a visual indicator (inset) on the chest of a jaundiced infant undergoing phototherapy treatment. (**D**) EQE spectrum of blue PD (n = 1) with and without a layer of PI (5 μm) and absorbance spectrum profile of bilirubin. (**E**) Voltage measurements of blue sensor (n = 1) as a function of total dose blue light phototherapy. Dosimeter (n = 1) was irradiated with constant intensity for 60 min at 30.0 and 9.3 μW/cm^2. (**F**) Voltage measurements of blue sensors (n = 3) as a function of blue light phototherapy intensity. Error bars represent the SD. (**G**) Measurements of instantaneous intensity and cumulative dosimetry from an mm-NFC device (n = 1) on the chest of a jaundiced infant throughout the course of a 20-hour phototherapy session.

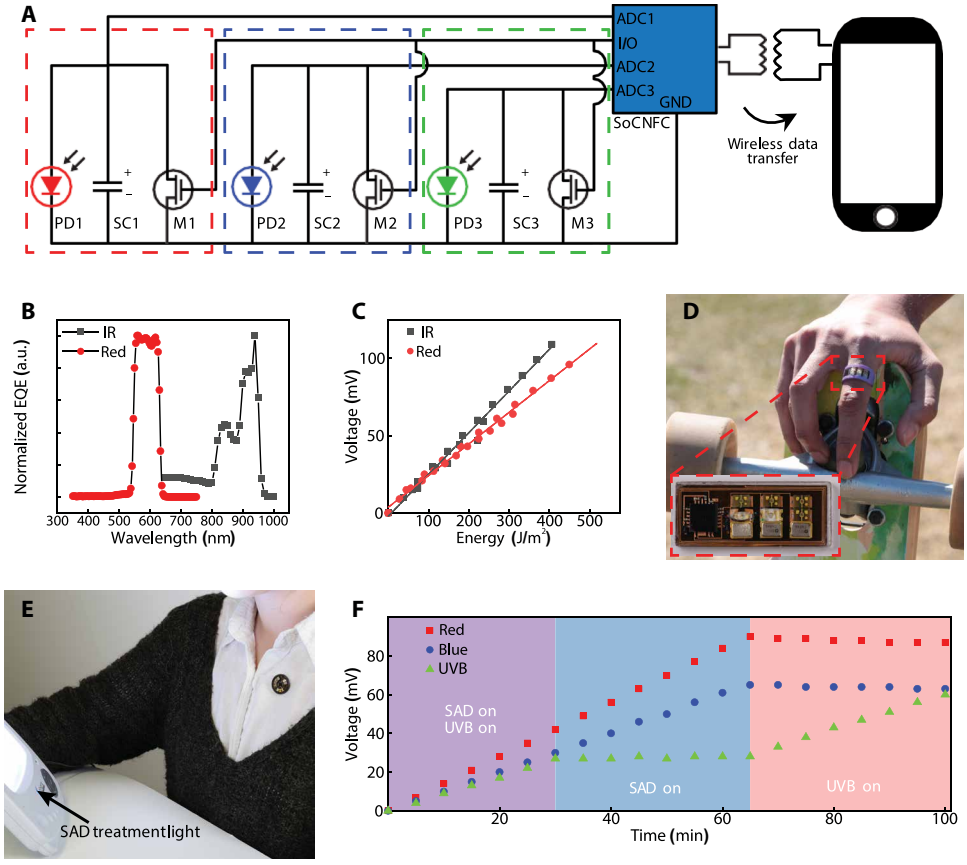

Fig. 6. mm-NFC dosimeters with separate, independent operation at IR to the UV wavelengths. (**A**) Circuit diagram of the device and wireless communication to a smartphone. The configuration uses three separate ADCs on a single NFC chip, three SCs (SC1, SC2, and SC3), three MOSFETs (M1, M2, and M3), a single GPIO for reset and three separate photodetectors (PD1, PD2, and PD3). (**B**) EQE spectrum of broadband red and IR PDs ($n = 1$). (**C**) Voltage measurements from an mm-NFC sensor ($n = 1$) operating in the IR/red as a function of exposed energy at each corresponding wavelength range. (**D**) Image of an mm-NFC dosimeter with operation in the UVA/UVB/IR configured as a ring. Inset shows higher magnification. (**E**) Image of an mm-NFC dosimeter with operation in the UVB/red/blue as a shirt-worn badge in front of a white light phototherapy lamp. (**F**) Results of cumulative dosimetry using a UVB/red/blue mm-NFC device ($n = 1$) during exposure with different light sources, illustrating stable, separate operation across corresponding regions of the spectrum.

a ring form (Fig. 6D) with a rectangular antenna (length, 21.5 mm; width, 8.7 mm) enables precise, localized, convenient monitoring of UV and IR exposures. Another area of interest in dosimetry focuses on visible light therapy for conditions such as seasonal affective disorder (SAD) (*27*, *28*). Figure 6E shows a device for red/blue/UVB dosimetry as a badge, a platform that integrates four UVB PDs, two blue PDs, and one red PD. Dosimetry in the red and blue spectral regions can quantify exposure to visible light from the sun and indoor lights throughout the day for users at risk for SAD. The UVB functionality can help to prevent overexposure to UVB while outdoors. Figure 6F demonstrates spectrally resolved UVB/red/blue monitoring during three phases of illumination: (i) a UVB (305 nm) lamp and a white light used in the treatment of SAD, (ii) only the SAD lamp, and (iii) only the UVB lamp. As with the previously described experiments with UVA and UVB lamps, to observe the effects of leakage, the reset was not activated at any point during the experiments. Results for red and blue dosimetry showed constant slopes throughout phases 1 and 2 (SAD lamp) and charging responses independent of UVB exposure. Leakage induced a reduction of ~3 mV in potential for the SCs for red and blue dosimetry during the 30 min of phase 3. A reset to minimize voltage across SC reduces the extent of signal decay over time. Results for UVB dosimetry exhibit a constant slope in phases 1 and 3 and a stable plateau in phase 2.

DISCUSSION

Wireless, millimeter-scale, body-worn dosimeters are versatile platforms for fully passive but continuous and accurate monitoring of light irradiation across the entire solar spectrum at single- or multiple-wavelength bands. Previously reported digital wearables for UV dosimetry restrict wearable locations to the wrist, chest, or the waist or to regions of clothing, through clips, that can accommodate the size and bulk of the devices. The miniature, thin, flexible, lightweight form factors of the battery-free devices reported here can conform robustly to curved surfaces to allow for dosimetry at body areas of critical interests such as bare shoulders and ears and on accessories such as sunglasses, with negligible burden.

These mm-NFC dosimetry platforms also eliminate the need for additional memory chips and batteries, as typically required in conventional systems. Here, measurements capture accumulated energy in a continuous, uninterrupted mode in the form of voltage that develops on an SC. Alternative technologies determine instantaneous intensities intermittently and then compute an effective cumulative exposure dose by numerical time integration using assumed linear variations in intensity between successive measurements. The accuracy in this mode degrades in scenarios where the intensity fluctuates faster than the sampling intervals. For instance, conventional wearables strapped to the wrist of a runner moving in and out of shade or a swimmer moving in and out of the water can yield inaccurate measurements of cumulative dose.

The accuracy of the mm-NFC platforms is primarily limited by the storage capacity of the SC and the associated parasitic leakage currents. To maintain a low SC bias and minimize leakage currents, a discharge command accompanies each wireless data acquisition event. In this way, mm-NFC dosimeters are reusable with an extendable detection range of accumulated doses. The willingness of users to monitor their sun exposure is a critical factor in achieving high-density and high-quality data.

A fundamental limitation of devices with designs reported here is the small detection area of the sensor relative to the surface area of a body. The results represent localized measurements of exposure, whereas the sun irradiance profile across the body surface is

not uniform and varies by position of the sun in the sky over the course of a day. An erect human outdoors receives the highest UV radiation at the vertex of the head, and the shoulders and nose receive 81 and 27% of the ambient radiation, respectively (*29*). Mounting on the fingernail represents one embodiment that offers a static, robust space with minimal irritation and optimal adhesion. However, exposure at the fingernail is not representative of exposure to the whole body. In the future, multinodal sensing with UVA/UVB dosimeters on the face, extremities, and trunk could be used to create anatomic specific risk assessment of UV exposure. In addition, careful selection of nonirritating, skin-safe adhesives for mounting on the skin is an important consideration.

The implications of this technology are not only in consumer health and clinical medicine in the context of sunburn and excessive exposure to UV but modified versions of these systems also allow dosimetry of up to three wavelengths, instantaneous and cumulative sensing in modes that can involve continuous wireless interrogation of the device, and operation with visual indicator lighting. In the context of blue light phototherapy for neonates, this functionality could improve protocols for the treatment of hyperbilirubinemia both in the NICU and outpatient settings. The daily cost of a NICU stay averages a median of US$1170 (*30*). A dosimeter that would facilitate faster discharge from the NICU by ensuring maximal phototherapy benefit would likely yield additional economic benefits.

Integration of PDs with sensitivity in the visible and IR ranges yields mm-NFC dosimeters with multimodal wavelength operation, important when considering oxidative stresses associated with IR and correlations of visible light exposures with moods and circadian rhythms. In addition to medical, cosmetic, and lifestyle applications, dosimetry can be important in occupational health monitoring for welders, steel workers, and others exposed to harmful UV, visible, and/or IR radiation. Recent studies suggest that measurements of UV and visible light aerosol optical depth can predict pollution concentration (*31*); these devices could act as sensors for the detection of local pollution concentration. Low-cost dosimeters—including the simplicity of operation, the ultraminiaturized size, the potential for scalable manufacturing, the battery-free construction, the completely sealed, waterproof design, the smartphone-compatible wireless communication protocol, the robust, long-lived operation, the absence of moving parts, and the diversity of functional modes—address multiple barriers to adoption across many different classes of applications.

MATERIALS AND METHODS

Study design

The objective of this study was to design, fabricate, and analyze battery-free, flexible, wireless dosimeters. Devices/patches were constructed from flexible copper substrate and off-the-shelf, surface-mount electronics and encapsulated with UV-transparent polymer. Devices were tested on healthy human participants outdoors (UV study) and jaundiced neonates (blue light study) in a clinical setting. The UV study in Rio, Brazil was approved by the L'Oreal Internal Ethical Committee. The study was sponsored by La Roche Posay and L'Oreal California Research Center (USA), with oversight by D. Moyal of France. The UV study in Florida was approved by the Loreal Institutional Review Board and overseen by J. V. Murray Jr. The blue light study was approved by the University of Illinois and Carle Hospital Institutional Review Board and overseen by D.R. The UV study evaluated the performance of battery-free, wireless dosimeters adhered on skin or mounted on a fingernail of volunteers engaging in outdoor activities including lounging, walking, and swimming. Users extracted wireless measurements of cumulative UV dosage from battery-free dosimeters using smartphones at instructed intervals. The blue light study demonstrated robust performance of battery-free, wireless, monitoring devices in the NICU environment. These devices epidermally adhered on the chest of three jaundiced infants undergoing blue light phototherapy for wireless and continuous measurements of blue light intensity and cumulative dosage over a 20-hour treatment period.

Fabrication of mm-NFC dosimeters

A sheet of PI (thickness, 75 μm) clad in rolled and annealed copper (thickness, 18 μm) served as the substrate for a flexible circuit board (AP8535R, Pyralux) with conductive traces defined by patterned ablation of the copper using a UV laser system (ProtoLaser U4, LPKF). A galvanic pulsed electroplater (Contac S4, LPKF) formed high–aspect ratio copper deposits through laser-ablated holes through the PI to bridge the front and back copper layers of the circuit substrate. In/Ag soldering paste (Ind. 290, Indium Corporation) attached surface-mount electrical components [SC, CPH3225A (Seiko Instruments); MOSFET, CSD17381F4 (Texas Instruments); UVA PD, SM1206UV (Bivar); UVB PD, GUVB-C21SD (GenUV); blue PD, XZM2DG55W (SunLED); Amp, ADA 4504–2 (Analog Devices); IR PD, VSMB10940 (Vishay Semiconductors); red PD, APDA3020 (Kingbright)] to the copper traces. A pick-and-place machine aligned SoC NFC (TRF430, Texas Instruments) for bonding using an anisotropic conductive paste (AC245, Delo Monopox) via defined pressure and temperature profiles. A CO_2 laser partially cut away the lens built onto the PD to minimize the thickness of this component before this mounting process. PDMS (Sylgard 184, DOW corning) cast and cured at 70°C across the top and bottom sides of the devices provided a waterproof and wear-resistant protective seal.

Calibration of dosimeters

Calibration involved UVA (UVL-26, Analytik Jena) and UVB (UVM-28, Analytik Jena) lamps with constant intensity output as sources for exposing the sensors inside a darkroom environment (C-10E6, Analytik Jena). UVA (Sensitive UVA Meter, Solarmeter) and UVB photometers (Sensitive UVB Meter, Solarmeter) measured the intensities at the point of exposure. Time integration of the exposure intensity measured in this way yielded the cumulative dosage of UVA and UVB exposure. A smartphone (Nexus 5) or an NFC reader (TRF7970AEVM, Texas Instruments) wirelessly acquired voltage measurements of the UV sensors.

For calibration of blue light sensors, a blue light phototherapy system (Giraffe Blue Spot PT, GE Healthcare) provided an exposure source, and a blue light meter (Bilirubin Meter, Solarmeter) measured the intensity at the point of exposure. For calibration of the red, green, and IR sensors, LEDs at the corresponding wavelengths served as exposure sources.

Smartphone application

A smartphone application was developed to wirelessly couple to battery-free, NFC dosimeters to extract and store device measurements and to reset the device. When an NFC-enabled smartphone scans an NFC dosimeter, the application reads and stores the voltage across one or more selected SCs (V_{sc}). The reset feature wirelessly drains SC charge and reads V_{sc} before and after charge drainage.

For the UV study, users collected V_{sc} at instructed intervals without reset using the application. The algorithm to compute cumulative exposure dose requires at least two sequential scan events before [*V*initial (*V*i)] and after exposure [*V*final (*V*f)] and an appropriate calibration factor. The accumulated SC voltage ($dV = Vf - Vi$) over elapsed time multiplied by a calibration factor represents exposure dosage of observed wavelength. User input of their skin type, activity level, and sun protection behavior can be coupled to real-world UV exposure to warn for impending sun damage using minimal erythema dose.

UV study

Outdoor human trials were conducted to assess the performance of mm-NFC UVA dosimeters in practical scenarios under controlled and uncontrolled exercise conditions in dry and aquatic environments. Two separate studies took place in Rio, Brazil and St. Petersburg, Florida. Field trials in St. Petersburg investigated NFC UVA dosimeters in epidermal patch format, and the study in Rio specifically explored the feasibility and durability of the NFC UVA dosimeters in fingernail formats. On days involving nonaquatic events, participants wore a commercial UV monitoring device on the wrist. The commercial UV radiometer designed to measure and store instantaneous intensity at a preprogrammed interval (30 s) consisted of a UVA PD, microprocessor, memory module, battery, and a large optical diffuser. Time integration of intensities yielded accumulated UV dosage. Each study recruited at least 10 physically fit male and female volunteers. The selected participants represented three different skin types classified on the basis of the Fitzpatrick scales IV to VI. The clinical study excluded pregnant females, individuals with history of skin cancer or abnormal response to sun, and/or participants known to consume photosensitizing drugs.

In St. Petersburg, Florida (26 August 2016; latitude, 27.8°N), each study participant wore four NFC UVA dosimeters on the LBH, LIA, LOA, and RBH. Each participant also wore a commercial UVA dosimeter on the right wrist. The participants walked a predetermined 4-mile route in a square pattern for an hour during the morning, noon, and the afternoon. The participants acquired data wirelessly from the NFC UVA dosimeters with a smartphone (Nexus 5) at 30-min intervals over the study period. The commercial dosimeter automatically sampled and stored data at a programmed interval but required docking to a computer for data transfer and display.

In Rio, Brazil (10 March 2016; latitude 22.0°S), each participant wore an NFC UVA dosimeter on the thumb or the middle finger and a commercial UVA dosimeter (Scienterra) on the wrist of the ipsilateral side. Participants collected data with a smartphone every hour. On days 1 and 2, the participants joined in recreational activities on a rooftop from 9 a.m. to 4 p.m. On the third day, the participants engaged in diverse activities in and around a pool from 8 a.m. to noon, including showering and swimming with the use of soap and skin creams. On day 4, the participants took part in swimming pool activities for 2 to 3 hours, with complete immersion of the sensors in water.

Blue light study

Clinical trials aimed to demonstrate functionality of mm-NFC blue light dosimeters in the NICU under incubation conditions of the infants. The study recruited three neonates undergoing blue light phototherapy treatments with parental consent. A standard blue light phototherapy system (Giraffe Blue Spot PT, GE Healthcare) served as the exposure source. For one especially colicky patient, Bili blanket (Datex Ohmeda Biliblanket, GE Healthcare) was wrapped around the neonate. Devices, NFC reader antenna (30 cm by 30 cm), and a data collection program were provided to the nurses with training and instructions. Nurses mounted the sensor with skin-safe adhesive on the chest of the patient at the beginning of the phototherapy. NFC reader antenna positioned underneath the incubator mattress, paired with a laptop to extract and record data, enabled automatic, wireless, and continuous measurements of blue intensity and blue dosage at a selected interval of 20 min over 20 hours. The neonates were handled as usual, and the nurses noted the position (supine, lying left, lying right, feeding, and cradling) of the infant hourly.

Statistical analysis

Data show means and SDs unless noted in the figure legends. The results of human trials in Florida omit four failed device measurements obtained with a smartphone during the exercise at afternoon. Linear regression analysis of measured sensor data generated calibration curves. Origin Pro computed R^2, and the slope of the linear fit was used to determine calibration factors.

SUPPLEMENTARY MATERIALS

www.sciencetranslationalmedicine.org/cgi/content/full/10/470/eaau1643/DC1

Fig. S1. Screenshots of the smartphone application.
Fig. S2. Millimeter-scale, battery-free, wireless sensors of UVA/UVB radiation.
Fig. S3. Electrical characterization and simulation.
Fig. S4. Field study results involving human participants outdoors in Rio, Brazil.
Fig. S5. Field study results from outdoor exercise involving human participants in St. Petersburg, Florida.
Fig. S6. Field study results from a morning exercise involving human participants in St. Petersburg, Florida.
Fig. S7. Field study results from an afternoon exercise involving human participants in St. Petersburg, Florida.
Fig. S8. Field study results from an evening exercise involving human participants in St. Petersburg, Florida.
Fig. S9. UVA dosimetry measurements performed with Scienterra and an mm-NFC UVA device during time-dependent simulated shading.
Fig. S10. Demonstration of the use of mm-NFC dosimeters with dual operations in the UVA and UVB spectrums in a clinical phototherapy unit.
Fig. S11. Clinical utility of blue light mm-NFC dosimeters in a NICU.
Table S1. mm-NFC dosimeters with dual operation in the UVA and UVB spectrums after UVA phototherapy in clinical phototherapy unit.
Table S2. mm-NFC dosimeters with dual operation in the UVA and UVB spectrums after UVB phototherapy in clinical phototherapy unit.
Table S3. Spatiotemporal map of clinical UVA phototherapy unit measured with mm-NFC dosimeters with dual operation in the UVA and UVB spectrums.
Table S4. Spatiotemporal map of clinical UVB phototherapy unit measured with mm-NFC dosimeters with dual operation in the UVA and UVB spectrums.

REFERENCES AND NOTES

1. G. P. Guy Jr., S. R. Machlin, D. U. Ekwueme, K. R. Yabroff, Prevalence and costs of skin cancer treatment in the U.S., 2002–2006 and 2007–2011. *Am. J. Prev. Med.* **48**, 183–187 (2015).
2. L. Rahib, B. D. Smith, R. Aizenberg, A. B. Rosenzweig, J. M. Fleshman, L. M. Matrisian, Projecting cancer incidence and deaths to 2030: The unexpected burden of thyroid, liver, and pancreas cancers in the United States. *Cancer Res.* **74**, 2913–2921 (2014).
3. M. R. Donaldson, B. M. Coldiron, No end in sight: The skin cancer epidemic continues, in *Seminars in Cutaneous Medicine and Surgery* (Frontline Medical Communications, 2011), vol. 30, pp. 3-5.
4. P. Jensen, S. Hansen, B. Møller, T. Leivestad, P. Pfeffer, O. Geiran, P. Fauchald, S. Simonsen, Skin cancer in kidney and heart transplant recipients and different long-term immunosuppressive therapy regimens. *J. Am. Acad. Dermatol.* **40**, 177–186 (1999).
5. R. Siegel, C. DeSantis, K. Virgo, K. Stein, A. Mariotto, T. Smith, D. Cooper, T. Gansler, C. Lerro, S. Fedewa, C. Lin, C. Leach, R. S. Cannady, H. Cho, S. Scoppa, M. Hachey, R. Kirch, A. Jemal, E. Ward, Cancer treatment and survivorship statistics, 2012. *CA Cancer J. Clin.* **62**, 220–241 (2012).
6. W. B. Goggins, H. Tsao, A population-based analysis of risk factors for a second primary cutaneous melanoma among melanoma survivors. *Cancer* **97**, 639–643 (2003).

7. N. S. Agar, G. M. Halliday, R. S. C. Barnetson, H. N. Ananthaswamy, M. Wheeler, A. M. Jones, The basal layer in human squamous tumors harbors more UVA than UVB fingerprint mutations: A role for UVA in human skin carcinogenesis. *Proc. Natl. Acad. Sci. U.S.A.* **101**, 4954–4959 (2004).
8. B. S. Paul, J. A. Parrish, The interaction of UVA and UVB in the production of threshold erythema. *J. Invest. Dermatol.* **78**, 371–374 (1982).
9. A. M. Holzer, M. Athar, C. A. Elmets, The other end of the rainbow: Infrared and skin. *J. Invest. Dermatol.* **130**, 1496–1499 (2010).
10. I. Kohli, S. Chaowattanapanit, T. F. Mohammad, C. L. Nicholson, S. Fatima, G. Jacobsen, N. Kollias, H. W. Lim, I. H. Hamzavi, Synergistic effects of long wavelength ultraviolet A1 and visible light on pigmentation and erythema. *Br. J. Dermatol.* **178**, 1173–1180 (2017).
11. S. Vandersee, M. Beyer, J. Lademann, M. E. Darvin, Blue-violet light irradiation dose dependently decreases carotenoids in human skin, which indicates the generation of free radicals. *Oxid. Med. Cell. Longev.* **2015**, 579675 (2015).
12. S. W. Lockley, E. E. Evans, F. A. Scheer, G. C. Brainard, C. A. Czeisler, D. Aeschbach, Short-wavelength sensitivity for the direct effects of light on alertness, vigilance, and the waking electroencephalogram in humans. *Sleep* **29**, 161–168 (2006).
13. S. W. Lockley, G. C. Brainard, C. A. Czeisler, High sensitivity of the human circadian melatonin rhythm to resetting by short wavelength light. *J. Clin. Endocrinol. Metab.* **88**, 4502–4505 (2003).
14. R. G. Stevens, G. C. Brainard, D. E. Blask, S. W. Lockley, M. E. Motta, Breast cancer and circadian disruption from electric lighting in the modern world. *CA Cancer J. Clin.* **64**, 207–218 (2014).
15. A. Lazar, C. Koehler, J. Tanenbaum, D. H. Nguyen, Why we use and abandon smart devices, in *Proceedings of the 2015 ACM International Joint Conference on Pervasive and Ubiquitous Computing* (ACM, 2015), pp. 635–646.
16. D. A. Epstein, J. H. Kang, L. R. Pina, J. Fogarty, S. A. Munson, Reconsidering the device in the drawer: Lapses as a design opportunity in personal informatics, in *Proceedings of the 2016 ACM International Joint Conference on Pervasive and Ubiquitous Computing* (ACM, 2016), pp. 829–840.
17. D. A. Epstein, M. Caraway, C. Johnston, A. Ping, J. Fogarty, S. A. Munson, Beyond abandonment to next steps: Understanding and designing for life after personal informatics tool use, in *Proceedings of the 2016 SIGCHI Conference on Human Factors in Computing Systems* (CHI, 2016), pp. 1109–1113.
18. S. Banerjee, E. G. Hoch, P. D. Kaplan, E. L. Dumont, A comparative study of wearable ultraviolet radiometers, in *Life Sciences Conference (LSC)* (IEEE, 2017), pp. 9-12.
19. H. Araki, J. Kim, S. Zhang, A. Banks, K. E. Crawford, X. Sheng, P. Gutruf, Y. Shi, R. M. Pielak, J. A. Rogers, Materials and device designs for an epidermal UV colorimetric dosimeter with near field communication capabilities. *Adv. Func. Mater.* **27**, 1604465 (2017).
20. J. Kim, P. Gutruf, A. M. Chiarelli, S. Y. Heo, K. Cho, Z. Xie, A. Banks, S. Han, K.-I. Jang, J. W. Lee, K.-T. Lee, X. Feng, Y. Huang, M. Fabiani, G. Gratton, U. Paik, J. A. Rogers, Miniaturized battery-free wireless systems for wearable pulse oximetry. *Adv. Funct. Mater.* **27**, 1604373 (2017).
21. J. Kim, A. Banks, H. Cheng, Z. Xie, S. Xu, K. I. Jang, J. W. Lee, Z. Liu, P. Gutruf, X. Huang, P. Wei, F. Liu, K. Li, M. Dalal, R. Ghaffari, X. Feng, Y. Huang, S. Gupta, U. Paik, J. A. Rogers, Epidermal electronics with advanced capabilities in near-field communication. *Small* **11**, 906–912 (2015).
22. J. Kim, G. A. Salvatore, H. Araki, A. M. Chiarelli, Z. Xie, A. Banks, X. Sheng, Y. Liu, J. W. Lee, K. I. Jang, S. Y. Heo, K. Cho, H. Luo, B. Zimmerman, J. Kim, L. Yan, X. Feng, S. Xu, M. Fabiani, G. Gratton, Y. Huang, U. Paik, J. A. Rogers, Battery-free, stretchable optoelectronic systems for wireless optical characterization of the skin. *Sci. Adv.* **2**, e1600418 (2016).
23. C. R. Roy, H. P. Gies, D. J. Lugg, S. Toomey, D. W. Tomlinson, The measurement of solar ultraviolet radiation. *Mutat. Res.* **422**, 7–14 (1998).
24. T. R. C. Sisson, N. Kendall, E. Shaw, L. Kechavarz-Oliai, Phototherapy of jaundice in the newborn infant. II. Effect of various light intensities. *J. Pediatr.* **81**, 35–38 (1972).
25. American Academy of Pediatrics Subcommittee on Hyperbilirubinemia, Management of hyperbilirubinemia in the newborn infant 35 or more weeks of gestation. *Pediatrics* **114**, 297–316 (2004).
26. G. Shin, A. M. Gomez, R. Al-Hasani, Y. R. Jeong, J. Kim, Z. Xie, A. Banks, S. M. Lee, S. Y. Han, C. J. Yoo, J.-L. Lee, S. H. Lee, J. Kurniawan, J. Tureb, Z. Guo, J. Yoon, S.-I. Park, S. Y. Bang, Y. Nam, M. C. Walicki, V. K. Samineni, A. D. Mickle, K. Lee, S. Y. Heo, J. G. McCall, T. Pan, L. Wang, X. Feng, T. I. Kim, J. K. Kim, Y. Li, Y. Huang, R. W. Gereau IV, J. S. Ha, M. R. Bruchas, J. A. Rogers, Flexible near-field wireless optoelectronics as subdermal implants for broad applications in optogenetics. *Neuron* **93**, 509–521.e3 (2017).
27. R. N. Golden, B. N. Gaynes, R. D. Ekstrom, R. M. Hamer, F. M. Jacobsen, T. Suppes, K. L. Wisner, C. B. Nemeroff, The efficacy of light therapy in the treatment of mood disorders: A review and meta-analysis of the evidence. *Am. J. Psychiatry* **162**, 656–662 (2005).
28. G. Glickman, B. Byrne, C. Pineda, W. W. Hauck, G. C. Brainard, Light therapy for seasonal affective disorder with blue narrow-band light-emitting diodes (LEDs). *Biol. Psychiatry* **59**, 502–507 (2006).
29. M. G. Kimlin, A. V. Parisi, N. D. Downs, Human UVA exposures estimated from ambient UVA measurements. *Photochem. Photobiol. Sci.* **2**, 365–369 (2003).
30. R. B. Russell, N. S. Green, C. A. Steiner, S. Meikle, J. L. Howse, K. Poschman, T. Dias, L. Potetz, M. J. Davidoff, K. Damus, J. R. Petrini, Cost of hospitalization for preterm and low birth weight infants in the United States. *Pediatrics* **120**, e1–e9 (2007).
31. B. N. Wenny, V. K. Saxena, J. E. Frederick, Aerosol optical depth measurements and their impact on surface levels of ultraviolet-B radiation. *J. Geophys. Res. Atmos.* **106**, 17311–17319 (2001).

Acknowledgments: We thank the staff of the Materials Research Laboratory at University of Illinois and of the NUFAB and NUANCE facilities at Northwestern University for assistance in this research. We thank A. Froelich of the Department of Dermatology's Phototherapy Unit at Northwestern University for assistance. **Funding:** Research reported in this publication was supported by the National Cancer Institute of the NIH under award number R44CA224658. The content is solely the responsibility of the authors and does not necessarily represent the official views of the NIH. The materials and engineering efforts were supported by the Center for Bio-Integrated Electronics of the Simpson Querrey Institute at Northwestern University. J.K. acknowledges the Research Program of National Research Foundation of Korea (NRF) funded by the Korean government (MSIT) (NRF-2018R1C1B5045524 and NRF-2017M3A9F1031270) and the Research Grant of Kwangwoon University in 2018. **Author contributions:** A.B., S.Y.H., J.K., H.A., and J.A.R. led the development of the concepts, designed the experiments, and interpreted the results. S.Y.H., P.G., S.X., and J.A.R. wrote the paper. S.Y.H. and J.K. led the experimental works with support from J.K.R., S.X., P.G., M.P., J.W.K., A.E.P.-A., K.-T.L., and Y.Y. P.W., R.P., Y.S., and G.B. designed and led the field studies. D.R. and C.G. led the clinical studies in NICU. **Competing interests:** A.B., J.A.R., G.B., R.P., and P.W. have commercial interests in the technology. International patent filing by University of Illinois at Urbana-Champaign; PCT/US2016/035331 "Alternative Approach to UV Sensing." S.X. reported paid consultation for Aclaris Therapeutics. **Data and materials availability:** All data associated with this study are present in the paper or the Supplementary Materials.

Submitted 14 May 2018
Accepted 9 November 2018
Published 5 December 2018
10.1126/scitranslmed.aau1643

Citation: S. Y. Heo, J. Kim, P. Gutruf, A. Banks, P. Wei, R. Pielak, G. Balooch, Y. Shi, H. Araki, D. Rollo, C. Gaede, M. Patel, J. W. Kwak, A. E. Peña-Alcántara, K.-T. Lee, Y. Yun, J. K. Robinson, S. Xu, J. A. Rogers, Wireless, battery-free, flexible, miniaturized dosimeters monitor exposure to solar radiation and to light for phototherapy. *Sci. Transl. Med.* **10**, eaau1643 (2018).

Science Translational Medicine

Wireless, battery-free, flexible, miniaturized dosimeters monitor exposure to solar radiation and to light for phototherapy

Seung Yun Heo, Jeonghyun Kim, Philipp Gutruf, Anthony Banks, Pinghung Wei, Rafal Pielak, Guive Balooch, Yunzhou Shi, Hitoshi Araki, Derrick Rollo, Carey Gaede, Manish Patel, Jean Won Kwak, Amnahir E. Peña-Alcántara, Kyu-Tae Lee, Yeojeong Yun, June K. Robinson, Shuai Xu and John A. Rogers

Sci Transl Med **10**, eaau1643.
DOI: 10.1126/scitranslmed.aau1643

Safer sun exposure

Almost all skin cancers are caused by excessive ultraviolet (UV) irradiation from the sun. Sunscreens can reflect or absorb UV light to protect skin from damage but do not provide a measure of UV exposure. Heo *et al.* developed flexible, wireless, battery-free dosimeters to monitor light exposure. Body-worn sensors on human participants recorded UVA exposure during recreational outdoor activities, including swimming. Sensors could be fabricated in different shapes and sizes, could capture UVA and UVB exposure for clinical phototherapy, and could measure blue light exposure on infants with jaundice during bilirubin phototherapy. This wireless sensor platform technology enables high precision tracking of instantaneous and cumulative light exposure.

Science Translational Medicine
AAAS

www.sciencetranslationalmedicine.org/cgi/content/full/10/470/eaau1643/DC1

Supplementary Materials for

Wireless, battery-free, flexible, miniaturized dosimeters monitor exposure to solar radiation and to light for phototherapy

Seung Yun Heo, Jeonghyun Kim, Philipp Gutruf, Anthony Banks, Pinghung Wei, Rafal Pielak, Guive Balooch, Yunzhou Shi, Hitoshi Araki, Derrick Rollo, Carey Gaede, Manish Patel, Jean Won Kwak, Amnahir E. Peña-Alcántara, Kyu-Tae Lee, Yeojeong Yun, June K. Robinson, Shuai Xu*, John A. Rogers*

*Corresponding author. Email: stevexu@northwestern.edu (S.X.); jrogers@northwestern.edu (J.A.R.)

Published 5 December 2018, *Sci. Transl. Med.* **10**, eaau1643 (2018)
DOI: 10.1126/scitranslmed.aau1643

This PDF file includes:

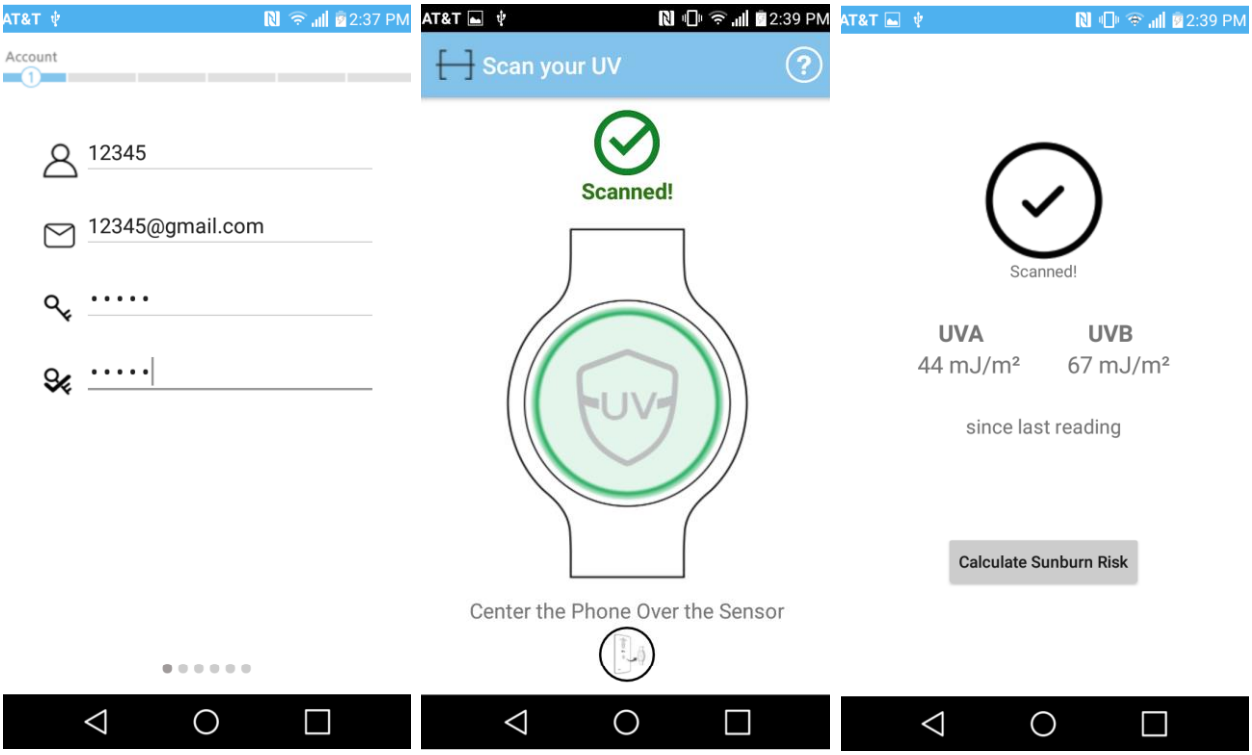

Fig. S1. Screenshots of the smartphone application. Wirelessly coupling a millimeter-scale, battery-free dosimeter to an NFC-enabled smartphone activates the device and the NFC communication link, resulting in a display of the measurement result on the screen of the smartphone. The app also features a reset command that activates the MOSFET to discharge the supercapacitor, thereby resetting the device.

Fig. S2. Millimeter-scale, battery-free, wireless sensors of UVA/UVB radiation. (A) Photographic images of mm-NFC UVA/UVB dosimeter as a skin patch mounted on shoulder, **(B)** mm-NFC UVA/UVB dosimeter as a shoe clip, **(C)** mm-NFC UVA/UVB dosimeter as a hair clip, **(D)** mm-NFC UVA dosimeter as a button, and **(E)** mm-NFC UVA dosimeter integrated into a hat.

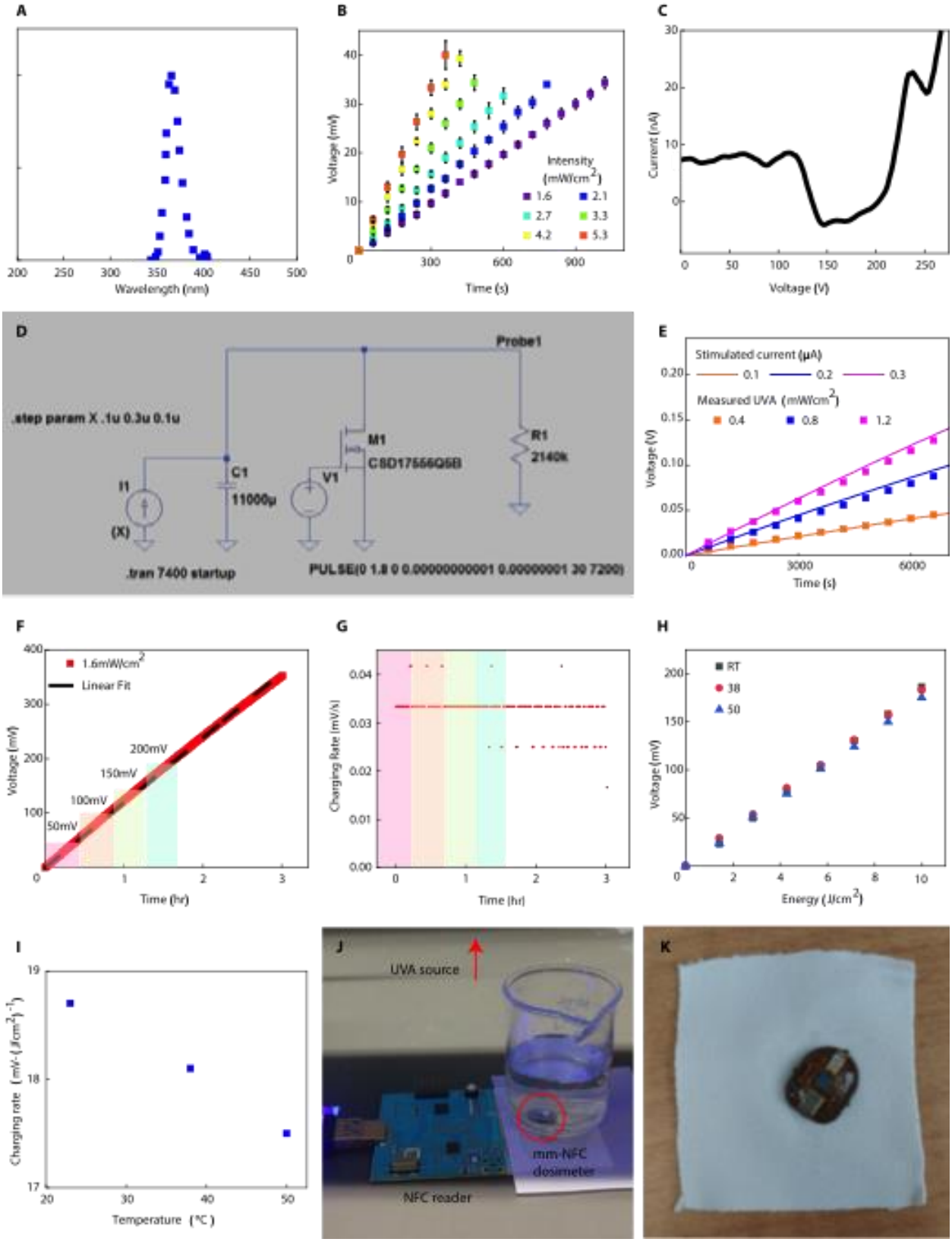

Fig. S3. Electrical characterization and simulation. (A) Spectral response of narrowband

UVA lamp with peak at 365 nm (UVL-16, Analytik Jena). **(B)** Voltage output as a function of time of UVA exposure measured with mm-NFC UVA dosimeters (n = 3). UVA lamp exposed dosimeters with constant intensity at six different intensities across a range from low to very high UVA index conditions outdoors. The error bars represent the standard deviation. **(C)** Current versus voltage response of analog to digital converter (ADC) of the NFC system-on-a-chip (n = 1) in the OFF state (no RF field applied), indicating leakage current to ground. **(D)** Schematic for the SPICE simulation of the circuit, where R1 represents a linear leakage current pathway. **(E)** Comparison of simulated and measured output voltages for the circuit. **(F)** Voltage response of mm-NFC UVA dosimeter (n = 1) with constant exposure over 3 hours. Readouts were wirelessly obtained every 10 minutes. **(G)** Derivative plot of voltage response in (E). **(H)** Voltage output of mm-NFC UVA (n = 1) as a function of cumulative energy measured at room temperature, 38°C, and at 50°C. **(I)** Respective charging rate of mm-NFC UVA (n = 1) as a function of temperature under constant exposure conditions. **(J)** Experimental setup of a mm-NFC UVA dosimeter submerged in heated water. The dosimeter was exposed to constant intensity of UVA as heated water cooled from 50°C to room temperature. Voltage and temperature readouts were obtained every 5 minutes with a reader antenna (not in contact with water). **(K)** Photograph of mm-NFC UVA dosimeter on a fabric swatch after an accelerated stress test in the washing machine.

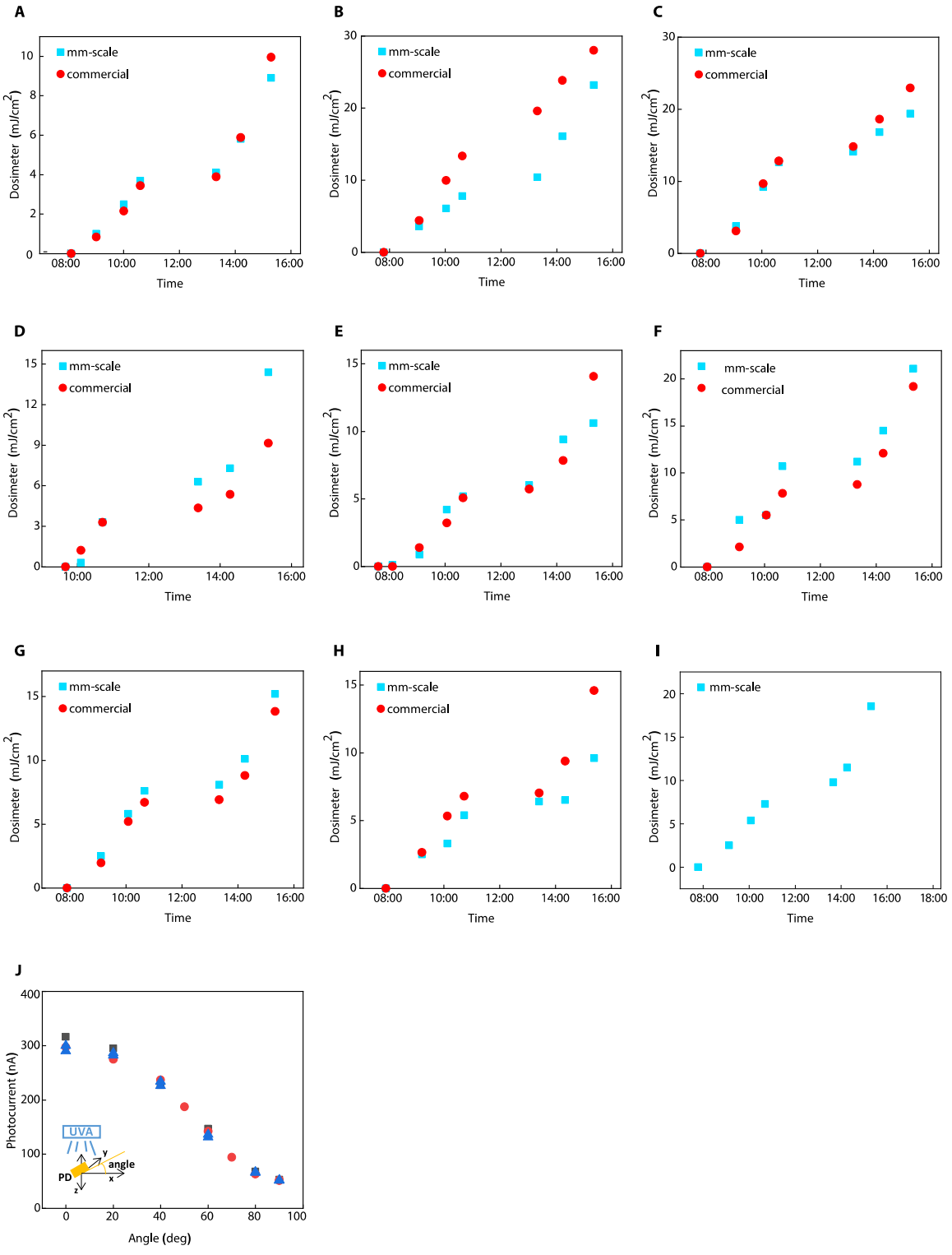

Fig. S4. Field study results involving human participants outdoors in Rio, Brazil. (A-I) Comparison of mm-NFC UVA dosimeter measurements to those of a standard commercial dosimeter from Scienterra. The measurements are from subjects (n = 9) in Rio, Brazil on the 10th

of March of 2016. Commercial dosimeter from one subject failed. Subjects wore one mm-NFC UVA dosimeter on the thumbnail or the middle fingernail, and one commercial dosimeter on the right wrist. Subjects engaged in preferred recreational activity of choice on a roof top. The voltage output of mm-NFC UVA dosimeters are scaled by a factor of 1000. One commercial dosimeter (I) failed during experiment. **(J)** Photocurrent from three UVA photodiodes as a function of orientation of photodiodes around y-axis with respect to UVA exposure source at constant orientation and intensity.

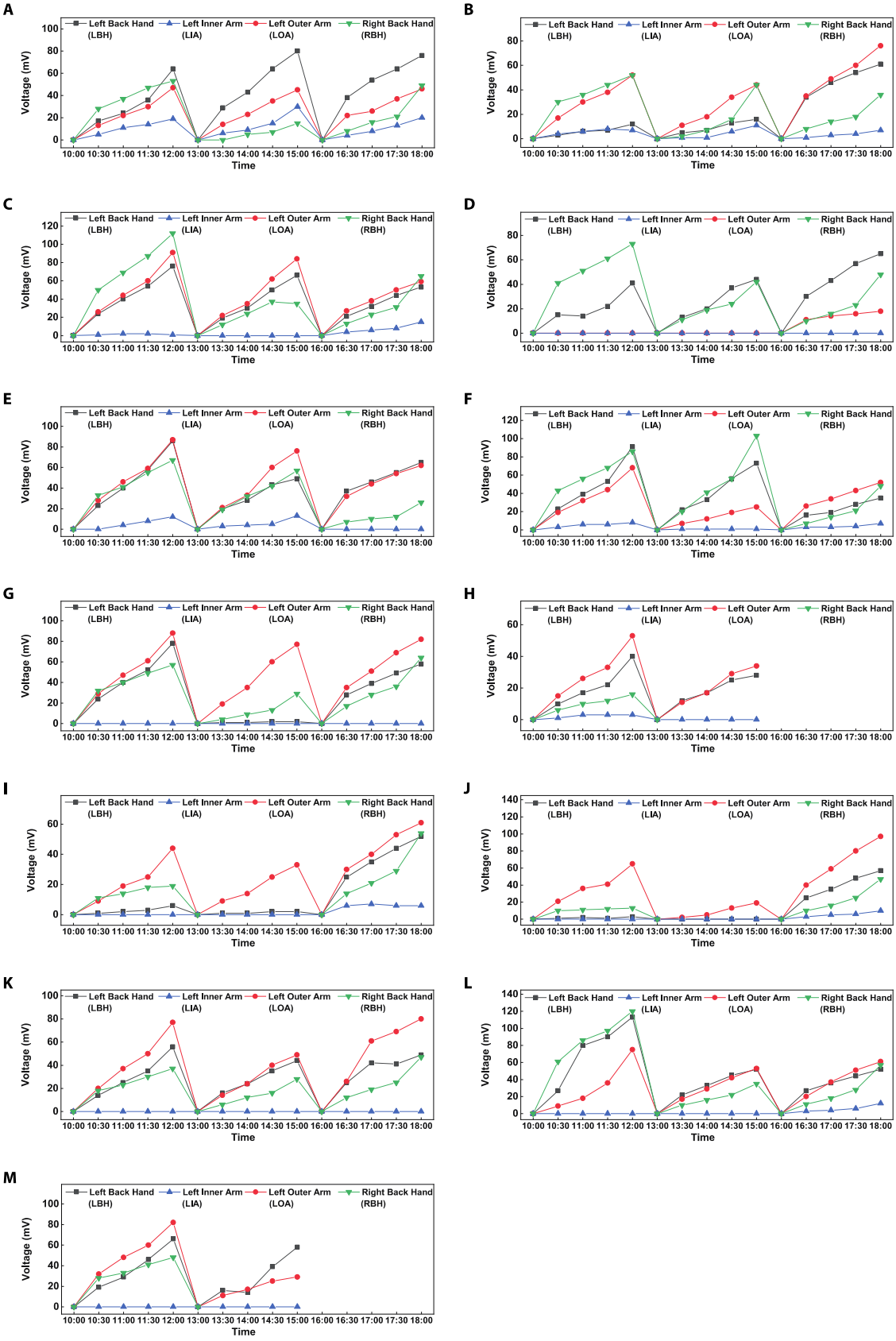
A
B
C
D
E
F
G
H
I
J
K
L
M
Left Back Hand (LBH)
Left Inner Arm (LIA)
Left Outer Arm (LOA)
Right Back Hand (RBH)
Voltage (mV)
Time
10:00 10:30 11:00 11:30 12:00 13:00 13:30 14:00 14:30 15:00 16:00 16:30 17:00 17:30 18:00

Fig. S5. Field study results from outdoor exercise involving human participants in St. Petersburg, Florida. (A-M) Individual level subjection data collected during an outdoor morning, afternoon and evening exercise sessions using mm-NFC dosimeters to those obtained with a commercial dosimeter. The measurements are from 13 study subjects in St. Petersburg, Florida on the August of 2016. Subjects wore mm-UVA NFC dosimeter patches on the right back hand (RBH), left back hand (LBH), left outer arm (LOA) and left inner arm (LIA). Four devices from RBH failed during an afternoon exercises. Measurements were acquired after walking north, east, west and south for approximately 30 minutes.

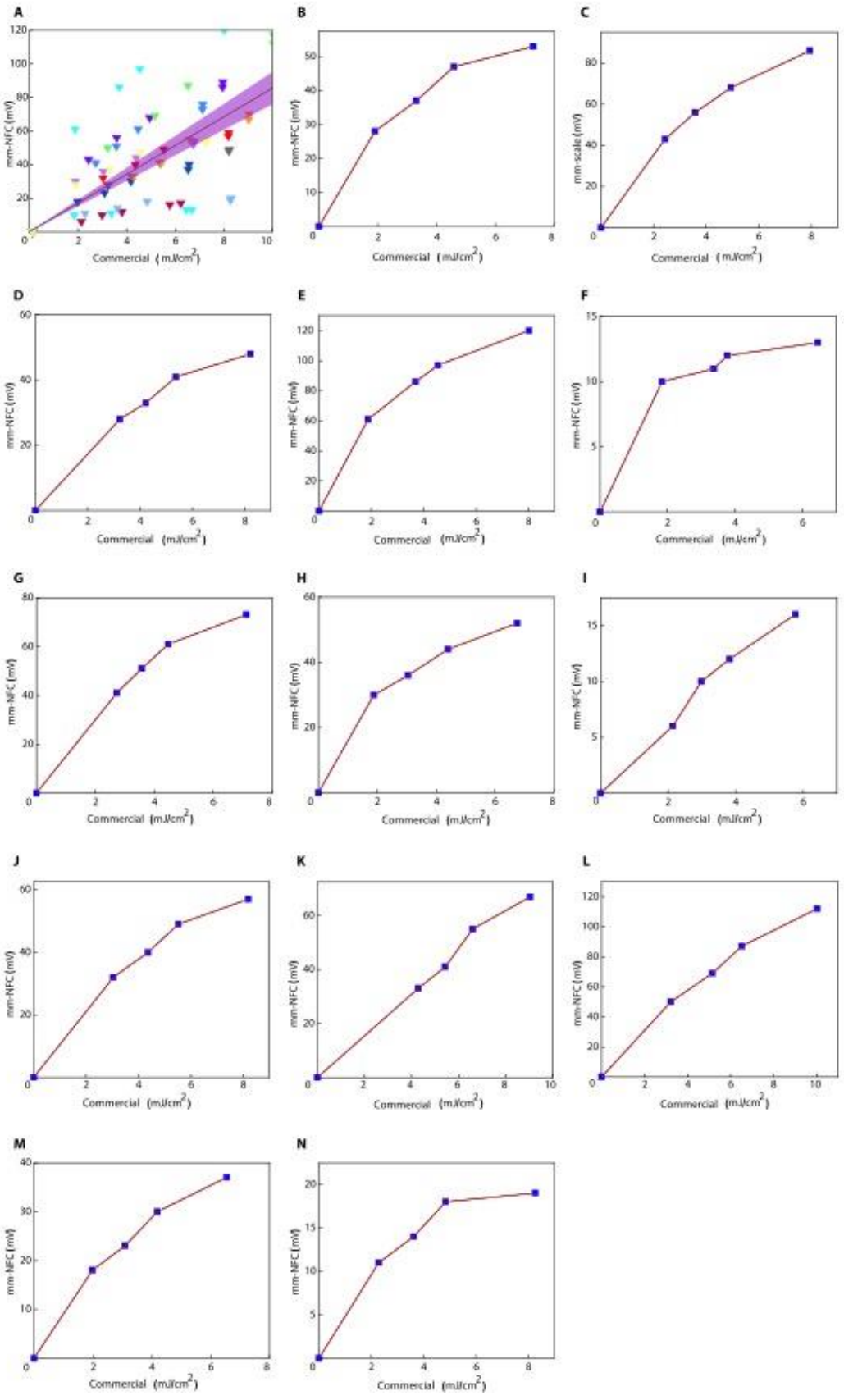
A
B
C
D
E
F
G
H
I
J
K
L
M
N
mm-NFC (mV)
mm-scale (mV)
Commercial (mJ/cm^2)

Fig. S6. Field study results from a morning exercise involving human participants in St. Petersburg, Florida. (A) Comparison of measurements collected during an outdoor morning exercise using mm-NFC dosimeters to those obtained with a commercial dosimeter. The measurements are from 13 study subjects in St. Petersburg, Florida on the August of 2016. Subjects wore mm-UVA NFC dosimeter patch on the right back hand and a commercial dosimeter on the ipsilateral wrist. Measurements were acquired after walking north, east, west and south for approximately 30 minutes. The graph includes a linear fit and a 95% confidence interval (shading). **(B-N)** Comparison of measurements collected during an outdoor morning exercise for individual subjects.

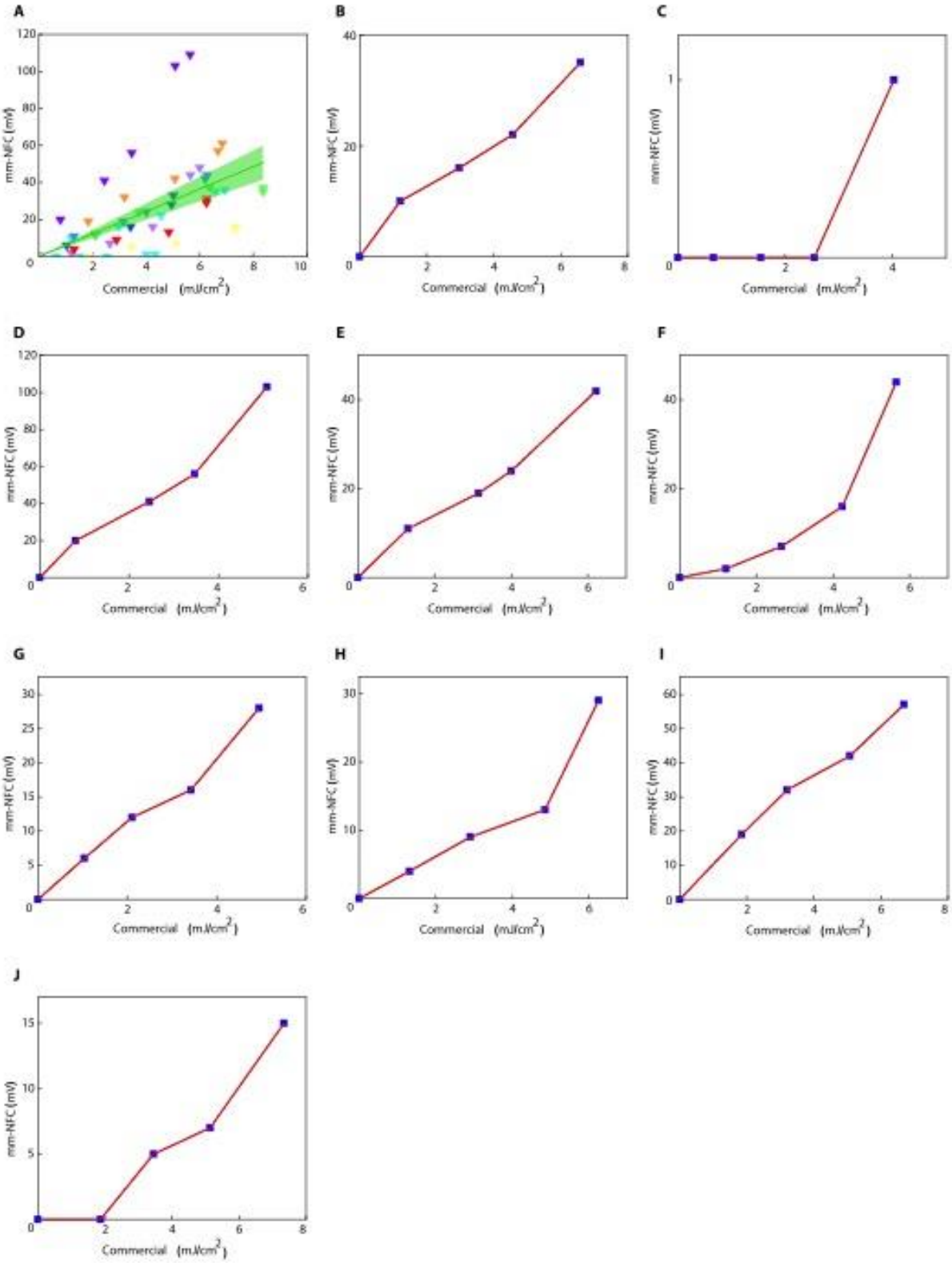

Fig. S7. Field study results from an afternoon exercise involving human participants in St.

Petersburg, Florida. (A) Comparison of measurements collected during an outdoor afternoon exercise using mm-NFC dosimeters to those obtained with a commercial dosimeter. The measurements are from 9 study subjects in St. Petersburg, Florida on the August of 2016. Subjects wore mm-UVA NFC dosimeter patch on the right back hand and a commercial dosimeter on the ipsilateral wrist. Four devices failed during testing (data not shown). Measurements were acquired after walking north, east, west and south for approximately 30 minutes. The graph includes a linear fit and a 95% confidence interval (shading). **(B-J)** Comparison of measurements collected during an outdoor afternoon exercise for individual subjects.

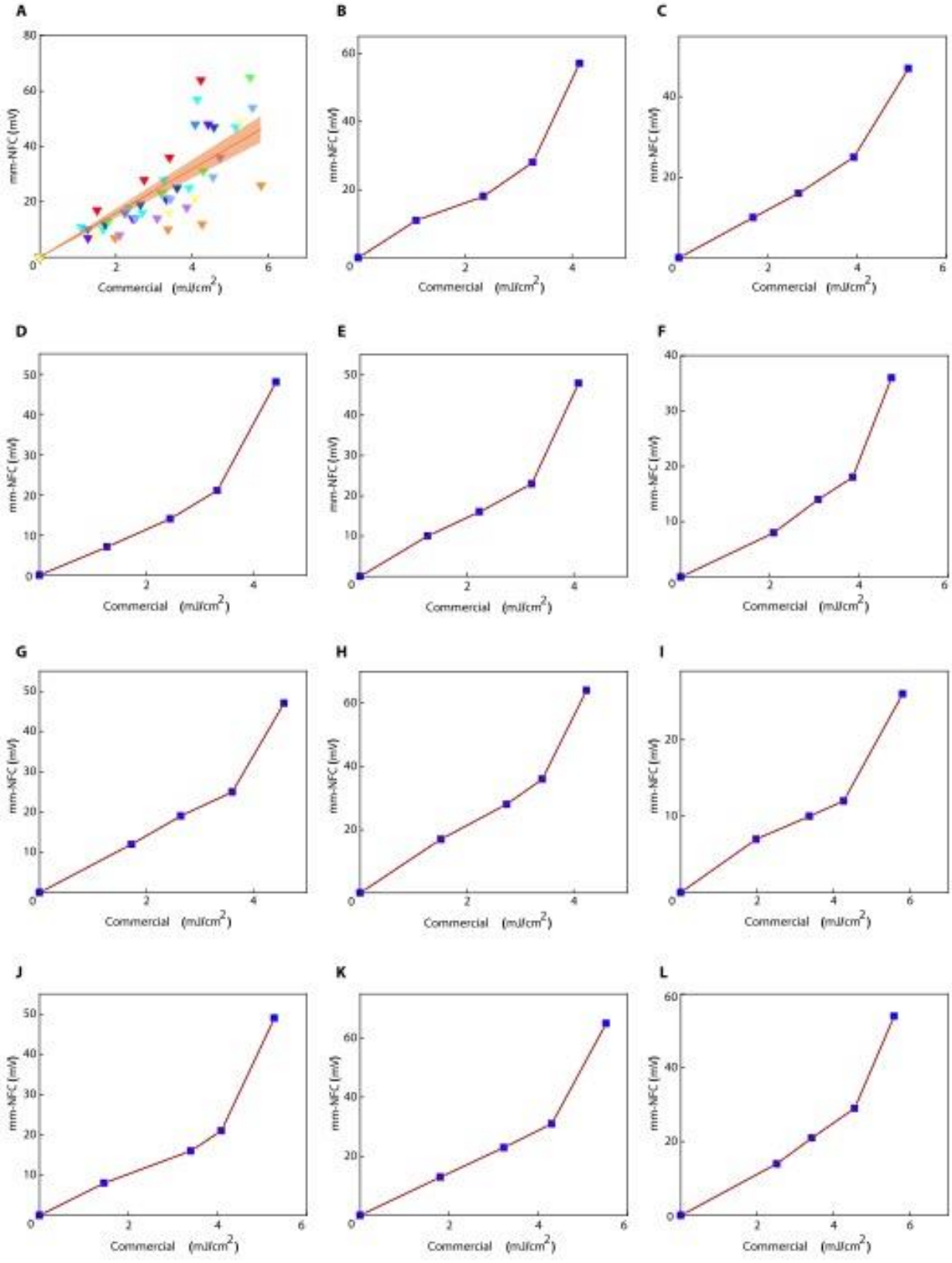
A
B
C
D
E
F
G
H
I
J
K
L
mm-NFC (mV)
Commercial (mJ/cm^2)

Fig. S8. Field study results from an evening exercise involving human participants in St. Petersburg, Florida. (A) Comparison of measurements collected during an outdoor evening exercise using mm-NFC dosimeters to those obtained with a commercial dosimeter. The measurements are from 11 study subjects in St. Petersburg, Florida on the August of 2016. Subjects wore mm-UVA NFC dosimeter patch on the right back hand and a commercial dosimeter on the ipsilateral wrist. Measurements are acquired after walking north, east, west and south for approximately 30 minutes. The graph includes a linear fit and a 95% confidence interval (shading). **(B-L)** Comparison of measurements collected during an outdoor evening exercise for individual subject.

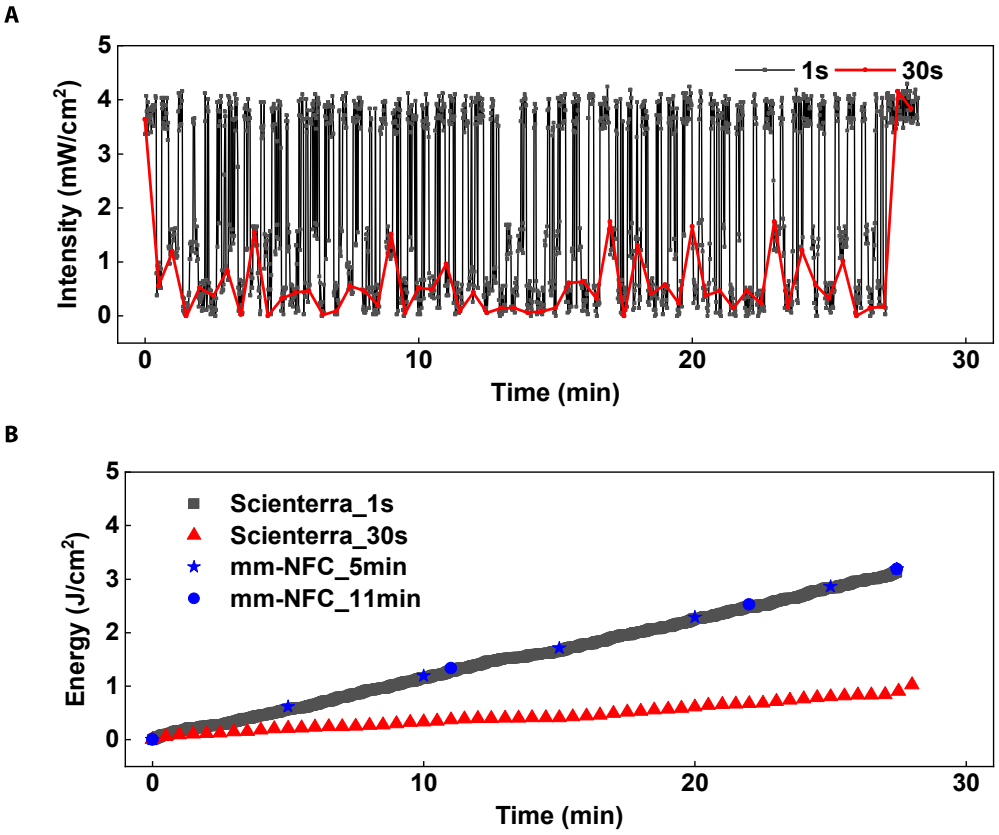

Fig. S9. UVA dosimetry measurements performed with Scienterra and an mm-NFC UVA device during time-dependent simulated shading. (A) UVA (395 nm) exposure intensity as a function of time measured by the Scienterra sensor (n = 1) operating with sampling intervals of 1 s and 30 s. Simulations involved absorbing films moved into and out of the light path between a UVA lamp and the devices, to simulate time depending shading. **(B)** Scienterra measurements of cumulative exposure dose computed by temporal integration of intensities over time sampled at 1 s (black) and 30 s (red), and corresponding results from mm-NFC UVA (n = 1) measurements of cumulative dose recorded every 5 min (blue; star) and 11 min (blue; circle).

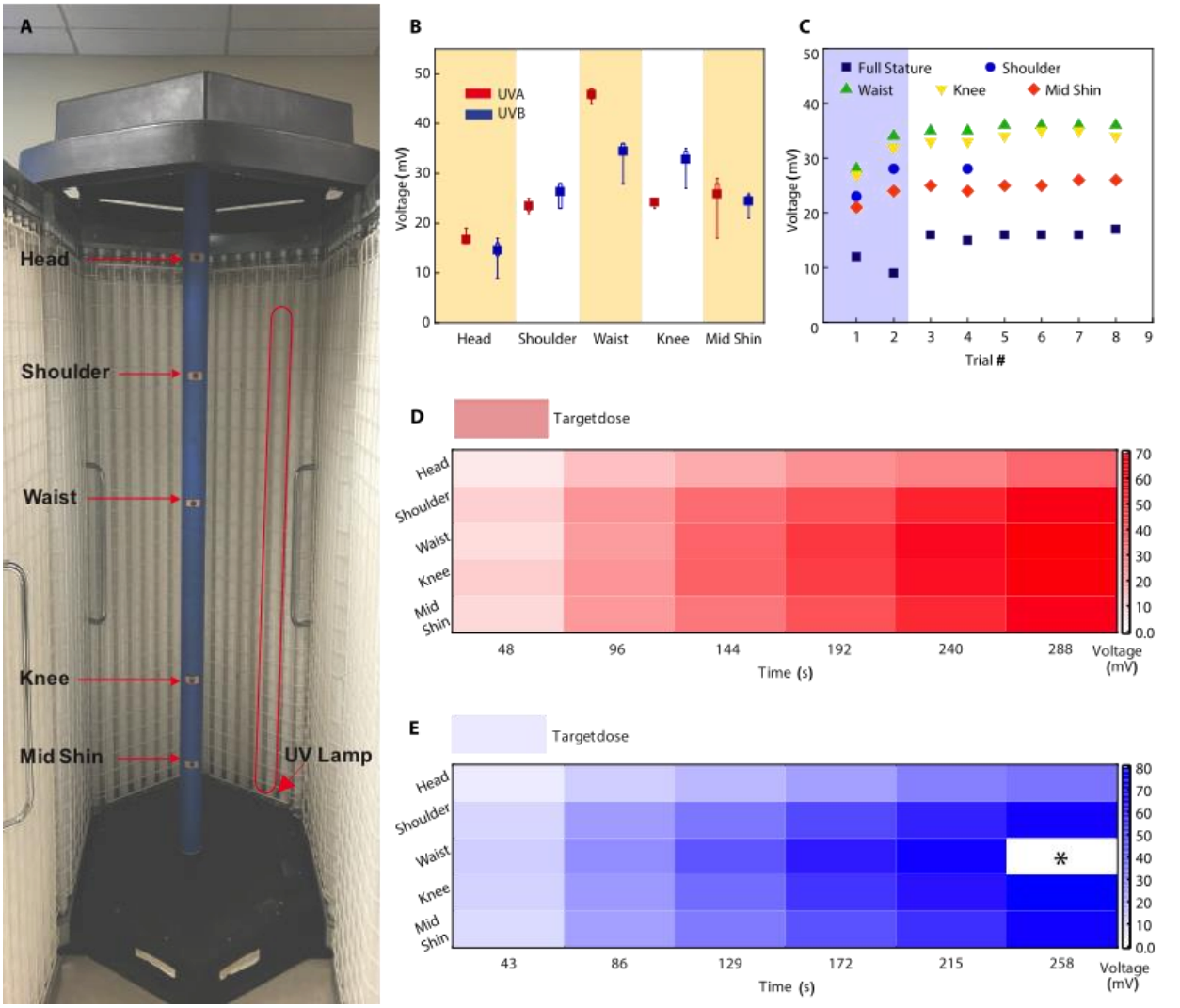

Fig. S10. Demonstration of the use of mm-NFC dosimeters with dual operations in the UVA and UVB spectrums in a clinical phototherapy unit. (**A)** Experimental setup of five dosimeters positioned along a vertical axis, corresponding to different anatomical locations, inside a UVB phototherapy unit. The sensor locations correspond to the average height of the head, shoulder, waist, knee and mid shin. **(B)** Box-and-whisker plot with minimum, maximum, 25%, 75% percentile, and mean of NFC dosimeter measurements (n = 8) from devices after phototherapy exposure to 21 mW/cm² of UVA (360 nm) for 238 s and to 4.6 mW/cm² UVB (311 nm) for 118 s. During UVB phototherapy session, the device at the shoulder failed (shoulder UVB; n = 3) **(C)** UVB dosimetry results from devices at five different height after UVB phototherapy (n = 8) under constant exposure conditions. The initial 2 trials highlight the warm-up phase of the UVB lamps. During UVB phototherapy session, the device at the shoulder failed (shoulder UVB; n = 3) **(D)** Color map of UVA dosimetry results from devices at five different heights after the UVA phototherapy. The reported results are means of 5 trials. **(E)** Color map of UVB dosimetry results from devices at five different heights after the UVB phototherapy. The results are means of 5 trials. One device failed (*).

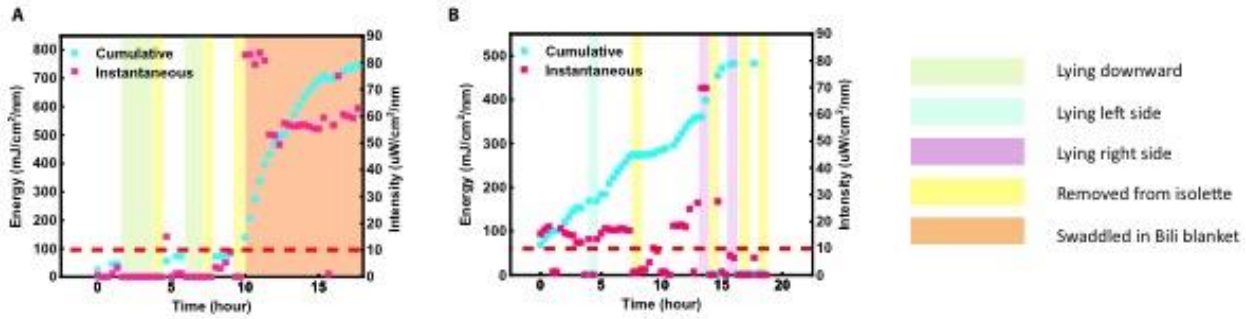

Fig. S11. Clinical utility of blue light mm-NFC dosimeters in a NICU. (A, B) Measurements of instantaneous intensity and cumulative dosimetry from mm-NFC blue light dosimeters mounted on the chests of three different jaundiced infants throughout the course of a 20 h phototherapy sessions. Shading indicates position or status of the neonate inside the incubator.

Table S1. mm-NFC dosimeters with dual operation in the UVA and UVB spectrums after UVA phototherapy in clinical phototherapy unit. Experimental setup of five dosimeters positioned along a vertical axis, corresponding to different anatomical locations, inside a UVA phototherapy unit. The sensor locations correspond to the average height of the head, shoulder, waist, knee and mid shin. NFC dosimeter measurements (n = 8) from devices after phototherapy exposure to 21 mW/cm² of UVA (360 nm) for 238 s.

Anatomical locations	Heights (in)	Measured UVA exposure (mV)							
		Trial 1	Trial 2	Trial 3	Trial 4	Trial 5	Trial 6	Trial 7	Trial 8
Full Stature	66.5	16	16	16	17	17	16	17	19
Shoulder	54.3	22	22	23	24	24	25	24	24
Waist	41.1	44	44	46	47	47	46	46	47
Knee	21	23	24	25	25	24	25	24	24
Mid shin	10	25	26	26	28	17	28	29	28

Table S2. mm-NFC dosimeters with dual operation in the UVA and UVB spectrums after UVB phototherapy in clinical phototherapy unit. Experimental setup of five dosimeters positioned along a vertical axis, corresponding to different anatomical locations, inside a UVB phototherapy unit. The sensor locations correspond to the average height of the head, shoulder, waist, knee and mid shin. NFC dosimeter measurements (n = 8) from devices after phototherapy exposure to 4.6 mW/cm² UVB (311nm) for 118 s. During UVB phototherapy session, the device at the shoulder failed (x).

Anatomical locations	Heights (in)	Measured UVB exposure (mV)							
		Trial 1	Trial 2	Trial 3	Trial 4	Trial 5	Trial 6	Trial 7	Trial 8
Full Stature	66.5	12	9	16	15	16	16	16	17
Shoulder	54.3	23	28	x	28	x	x	x	x
Waist	41.1	28	34	35	35	36	36	36	36
Knee	21	27	32	33	33	34	35	35	34
Mid shin	10	21	24	25	24	25	25	26	26

Table S3. Spatiotemporal map of clinical UVA phototherapy unit measured with mm-NFC dosimeters with dual operation in the UVA and UVB spectrums. Experimental setup of five dosimeters positioned along a vertical axis, corresponding to different anatomical locations, inside a UVA phototherapy unit. The sensor locations correspond to the average height of the head, shoulder, waist, knee and mid shin. NFC dosimeter measurements (n = 5) from devices after phototherapy exposure to 21 mW/cm² of UVA (360 nm) over time.

		UVA phototherapy time (s)																													
		48					96					144					191					239					287				
	Trial #	1	2	3	4	5	1	2	3	4	5	1	2	3	4	5	1	2	3	4	5	1	2	3	4	5	1	2	3	4	5
Measured UVA exposure (mV)	**Full stature**	5	3	7	5	6	18	11	12	16	13	17	22	17	21	20	24	25	25	23	28	30	29	28	31	27	34	34	31	34	34
	Shoulder	8	9	13	10	8	27	22	21	27	21	32	33	32	37	34	43	44	47	42	41	53	52	50	55	51	64	65	64	62	62
	Waist	5	8	6	7	6	21	22	24	22	23	37	37	35	39	34	48	49	50	46	47	61	57	55	60	57	69	73	67	72	69
	Knee	9	12	9	11	12	25	22	22	26	23	36	41	33	41	35	48	45	49	46	44	59	58	52	59	59	68	72	66	69	65
	Mid shin	6	9	8	12	7	24	22	21	27	23	27	30	32	35	31	41	38	40	40	39	50	52	44	53	49	58	63	57	62	58

Table S4. Spatiotemporal map of clinical UVB phototherapy unit measured with mm-NFC dosimeters with dual operation in the UVA and UVB spectrums. Experimental setup of five dosimeters positioned along a vertical axis, corresponding to different anatomical locations, inside a UVB phototherapy unit. The sensor locations correspond to the average height of the head, shoulder, waist, knee and mid shin. NFC dosimeter measurements (n = 5) from devices after phototherapy exposure to 4.6 mW/cm² UVB (311nm) over time. During UVB phototherapy session, the device at the waist failed (x).

		UVB phototherapy time (s)																													
		43					87					130					174					217					261				
	Trial #	1	2	3	4	5	1	2	3	4	5	1	2	3	4	5	1	2	3	4	5	1	2	3	4	5	1	2	3	4	5
Measured UVB exposure (mV)	**Full stature**	4	5	5	6	6	12	14	12	9	11	19	18	18	20	17	25	25	24	25	23	36	33	29	31	29	38	35	37	35	34
	Shoulder	7	11	10	11	11	24	26	24	23	26	36	34	37	37	33	47	47	50	48	48	59	63	56	61	55	76	67	75	70	68
	Waist	9	12	13	14	14	28	32	29	29	29	45	44	47	44	42	63	60	62	58	61	71	77	69	71	x	76	x	x	x	x
	Knee	9	11	12	11	12	23	30	24	25	26	40	35	42	37	35	55	49	55	49	56	59	70	57	69	57	83	67	82	83	77
	Mid shin	8	9	10	10	10	23	26	24	19	26	32	36	35	32	32	46	41	49	43	48	53	57	51	62	54	75	59	73	72	71